



Green synthesis, structure, cations distribution and bonding characteristics of superparamagnetic cobalt-zinc ferrites nanoparticles for Pb(II) adsorption and magnetic hyperthermia applications

Tetiana Tatarchuk^{a,b,c,*}, Alexander Shyichuk^{a,d}, Zbigniew Sojka^e, Joanna Gryboś^e, Mu. Naushad^{f,g}, Volodymyr Kotsyubynsky^h, Maria Kowalska^d, Sylwia Kwiatkowska-Marks^d, Nazarii Danyliuk^b

^a Department of Chemistry, Vasyl Stefanyk Precarpathian National University, 57 Shevchenko Street, 76018 Ivano-Frankivsk, Ukraine

^b Educational and Scientific Center of Material Science and Nanotechnology, Vasyl Stefanyk Precarpathian National University, Ivano-Frankivsk 76018, Ukraine

^c School of Life and Allied Health Sciences, Glocal University, Saharanpur, India

^d Faculty of Chemical Technology and Engineering, UTP University of Science and Technology, 3, Seminaryjna str., 85-326 Bydgoszcz, Poland

^e Faculty of Chemistry, Jagiellonian University, ul. Gronostajowa 2, 30-387, Krakow, Poland

^f Department of Chemistry, College of Science, Building #5, King Saud University, Riyadh 11451, Saudi Arabia

^g Yonsei Frontier Lab, Yonsei University, Seoul, Korea

^h Department of Material Science and New Technology, Vasyl Stefanyk Precarpathian National University, 57, Shevchenko Str., Ivano-Frankivsk 76018, Ukraine

ARTICLE INFO

Article history:

Received 12 December 2020

Received in revised form 3 January 2021

Accepted 9 January 2021

Available online 16 January 2021

Keywords:

Cobalt-zinc ferrites

Spinel

Adsorption

Lead

Magnetic hyperthermia

ABSTRACT

A simple “green” method for the synthesis of cobalt-zinc ferrites nanoparticles has been proposed. XRD, SEM/EDX, TEM, Mössbauer and FTIR techniques have been applied to investigate structure and morphology of the obtained spinel ferrites. Analysis of the cation distribution showed that during the transition from cobalt ferrite to zinc ferrite the inversion degree of the Fe cations decreases from $\delta = 0.89$ to $\delta = 0.00$. IR spectra show the presence of characteristic peaks of the M_A-O (at $\sim 450\text{ cm}^{-1}$) and M_B-O (at $\sim 610\text{ cm}^{-1}$) vibrations as well as the vibrations of functional groups of the honey residuals. It was concluded that honey acts as reductant and stabilizer preventing agglomeration of the nanoparticles. The force constants of the tetrahedral and octahedral bonds have been calculated. Dependence of the Debye temperature on Zn content was also established for the first time: it is increased from 782 K to 805 K with Zn increasing. It was shown that the ZnFe_2O_4 sample exhibits the highest adsorption capacity (289 mg/g) towards lead cations. This result is explained in terms of surface acidity of the examined samples, estimated from the variations of the ionic-covalent bond parameter. The Langmuir, Freundlich and Dubinin-Radushkevich models were tested to evaluate the adsorption mechanism. The efficiency of heat release by the $\text{Co}_x\text{Zn}_{1-x}\text{Fe}_2\text{O}_4$ magnetic nanoparticles for magnetic hyperthermia was investigated as well. The registered induction heating curves depend on the Zn content in the $\text{Co}_x\text{Zn}_{1-x}\text{Fe}_2\text{O}_4$ samples. The sample with $x(\text{Zn}) = 0.6$ exhibits the maximal specific loss power equal to 2.56 W/g. The intrinsic loss power (ILP) value is 0.40, and is 2.7 times higher than the ILP value of commercial Fe_3O_4 . The obtained ferrite materials can be, therefore, used in magnetic hyperthermia applications and Pb(II) adsorption.

© 2021 Elsevier B.V. All rights reserved.

1. Introduction

In the last decade, an exponential growth is observed in studies on magnetic spinel nanoparticles. Magnetic properties of spinels lead to their applications in microelectronics, optics, catalysis, medicine, as well as for the chemical sensors and environmental purposes, described in original papers [1–3]. Synthesis and application of magnetic nanoparticles are reviewed elsewhere [4–6]. Biomedical applications in vivo

include contrast materials for diagnostic nuclear magnetic resonance imaging, hyperthermia with alternating magnetic field, specific binding and target delivery of therapeutic agents as well as tissue engineering [7]. Magnetic spinels are promising adsorbents for removal of heavy metals, dyes, antibiotics, pesticides and other contaminants etc. [1,8–10]. Their main advantage is an easy separation from the spent solution using an external magnetic field instead of traditional centrifugation and filtration, which greatly simplifies and speeds up the overall process [4,11]. Surface of spinel magnetic sorbents can be modified with inorganic, organic or polymer substances, creating functional charged core-shell structures [12].

The chemical formula of ferrite spinels can be represented as MFe_2O_4 , where M is a divalent metal cation. The most valuable magnetic

* Corresponding author at: Department of Chemistry, Vasyl Stefanyk Precarpathian National University, 57 Shevchenko Street, 76018 Ivano-Frankivsk, Ukraine.

E-mail addresses: tatarchuk.tetyana@gmail.com (T. Tatarchuk), szyczuk@utp.edu.pl (A. Shyichuk), sojka@chemia.uj.edu.pl (Z. Sojka), mnaushad@ksu.edu.sa (M. Naushad).

properties are inherent for solid solutions formed by two ferrites, one of which is ferromagnetic (for example NiFe_2O_4 , MnFe_2O_4 , CoFe_2O_4), and the other is non-magnetic (for example ZnFe_2O_4) [13,14]. In such ferrites, zinc cations in the spinel structure usually occupy tetrahedral sites, while ferric cations are located in both tetrahedral and octahedral sites. The substituted zinc ferrite spinels can be described by the more general formula: $(\text{Zn}_x^{2+}\text{Fe}_{1-x}^{3+})_A(\text{M}_{1-x}^{2+}\text{Fe}_{1+x}^{3+})_B(\text{O}_4)_O$, where x is zinc molar fraction. Incorporation of the zinc ions into ferrite crystal lattice is accompanied by displacement of the iron cations from the tetrahedral (A) sublattice to the octahedral (B) sublattice. Thus, magnetization of the tetrahedral (A) sublattice decreases. Compensation between magnetic moments of the cations located in different sublattices (A and B) decreases. As a result, the overall magnetization of the samples increases. Consequently, the introduction of a nonmagnetic ions (such as Zn) into ferrite spinel structure leads to increase in the saturation magnetization [15]. Due to changes in the magnetic properties, mixed cobalt-zinc ferrites are very promising materials [16–18]. Cobalt-zinc ferrites have been investigated as catalysts [19,20], photo-catalysts [21], materials for hyperthermia [22], MRI contrast agents [23], antibacterial agents [24] etc.

A variety of chemical methods can be used to obtain spinel magnetic nanoparticles: sol-gel synthesis, synthesis in microemulsions, coprecipitation method, hydrothermal method, sonochemical methods [25–27]. Properties of the nanoparticles (composition, reproducibility, morphology and particle size distribution, specific surface and magnetic characteristics) depend on the particular synthesis method used. The size and shape of nanoparticles can be varied by adjusting pH, ionic strength, temperature and nature of the precursor metal salts (chlorides, sulfates, nitrates). Nanoparticle size effects their colloidal stability – the larger particle size, the faster its sedimentation [28,29]. Particle size distribution is important for biomedical applications. In the last years, “green” synthesis methods have become widespread [30–32]. “Green” synthesis protocols make possible to obtain nanoparticles of various shapes, sizes and structures. Typical “green” materials for these synthesis are plant extracts, fruits, vegetables, dairy products etc. [24,33–35]. Plants contain compounds that cause reduction of metal cations and formation of nanoparticles. Moreover, diversity of plants causes significant differences in composition of the extracts and may provide additional opportunities for obtaining nanoparticles differing in size, shape, surface composition and other characteristics [30]. For example, the well-known reducing agents are polyphenols, carotenoids, caffeine, tea and lemon extracts [30]. The obtained nanoparticles can be used in medicine as antimicrobial agents and for antitumor therapy [36–38].

“Green synthesis” with honey as a stabilizer is relatively new concept. Additionally reducing power of honey is used in synthesis of metallic gold, silver, platinum and palladium nanoparticles [39–43]. Specific properties of honey make possible to use it also in the synthesis of oxide nanoparticles [44,45]. Synthesis methods with honey as a stabilizer and reducing agent have a number of advantages. Honey contains many carbohydrates and vitamins, which are mild reducing agents and allow for controlling the size of nanoparticles. Additionally, honey proteins are stabilizers preventing nanoparticles from agglomeration. They are adsorbed during synthesis and have stabilizing effect due to electrostatic charge of the particle surface.

The aim of this work is to develop a simple “green” method for synthesis of chemically modified magnetic nanoparticles of cobalt-zinc ferrites, to study their adsorption properties and possibility of application in magnetic hyperthermia. Heavy metals are dangerous environmental pollutants, therefore, their complete removal is an important task in water purification [46–48]. The effect of cation substitution on sorption properties of the spinel ferrites has been reported previously [1,49]. It has been shown that cation substitution has an impact on the structure, morphology and adsorption activity of the nanoparticles [50]. Various magnetic adsorbents are used for Pb(II) adsorption, including graphene oxide/ NiFe_2O_4 composite [51], chitosan/ Fe_3O_4 nanocomposite [52], MnFe_2O_4 [53], MFe_2O_4 (where $M = \text{Co}, \text{Ni}, \text{Cu}, \text{Zn}$) [54,55], zinc

Table 1
The charges of chemical elements of the precursors.

Reagent	Calculations	Total charge
Cobalt(II) nitrate	$1 \times (+2) + 2 \times (1 \times (0) + 3 \times (-2))$	- 10
Zinc nitrate	$1 \times (+2) + 2 \times (1 \times (0) + 3 \times (-2))$	- 10
Ferric nitrate	$1 \times (+3) + 3 \times (1 \times (0) + 3 \times (-2))$	- 15
Glucose $\text{C}_6\text{H}_{12}\text{O}_6$	$6 \times (+4) + 12 \times (+1) + 6 \times (-2)$	+ 24
Fructose $\text{C}_6\text{H}_{12}\text{O}_6$	$6 \times (+4) + 12 \times (+1) + 6 \times (-2)$	+ 24

ferrite-alginate beads [56]. Zinc ferrite and cobalt ferrite as well as their composites are very popular adsorbents for removal of heavy metals, toxic dyes, pharmaceuticals or oil [55,57–62]. However, investigations into the adsorption properties of cobalt-zinc ferrites towards Pb (II) ions are absent so far. This study describes honey-mediated synthesis of cobalt-zinc NPs along with thorough characterization of their structure, particle size, morphology and chemical composition by various techniques (XRD, SEM/TEM, EDS, FTIR, Raman and Mössbauer techniques).

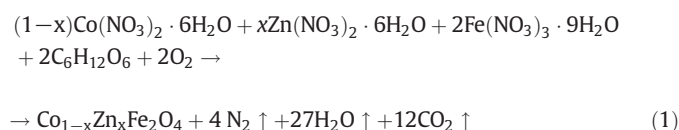
2. Experimental

2.1. Materials

Analytical grade zinc(II) nitrate hexahydrate $\text{Zn}(\text{NO}_3)_2 \cdot 6\text{H}_2\text{O}$, cobalt (II) nitrate hexahydrate $\text{Co}(\text{NO}_3)_2 \cdot 6\text{H}_2\text{O}$, ferric nitrate nonahydrate $\text{Fe}(\text{NO}_3)_3 \cdot 9\text{H}_2\text{O}$ were used for the synthesis of ferrite NPs. Honey of floral origin was used as stabilizing and reducing agent. The detailed characterization of honey functional groups was performed by FTIR spectroscopy (see Section 3.1).

2.2. Honey-mediated synthesis of cobalt-zinc ferrites

Stoichiometric amounts of the corresponding metal salts were dissolved in 75 mL of distilled water and stirred for 30 min. The honey was also dissolved in 75 mL of hot (50 °C) distilled water. The needed amount of honey has been calculated using the stoichiometric coefficient (ϕ_e), which indicates the oxidant/reductant ratio. In our study $\phi_e = 1$. In a first approximation, two main components of honey are glucose ($\text{C}_6\text{H}_{12}\text{O}_6$) and fructose ($\text{C}_6\text{H}_{12}\text{O}_6$), which act as the reducing agents. Taking into account the formal charges of the involved elements ($V(\text{C}) = +4$; $V(\text{H}) = +1$; $V(\text{O}) = -2$; $V(\text{N}) = 0$; $V(\text{M}) = +2$ or $+3$ (for M(II) or (M(III) respectively)), the charges of the precursors were calculated (see Table 1). The honey amount for synthesis was calculated using the oxygen balance equation. The solution of honey was added to the precursor metal salts solution and heated at 60 °C for 30 min under continuous stirring. After that, the solution was heated to boiling. Heating of the precursor solution led to decomposition of the honey monosaccharides. During the boiling, the solution turned into a sol and then into a gel, and then ignited spontaneously. As a result of such combustion synthesis, the ferrite nanopowder is formed, and this process is accompanied by release of N_2 , CO_2 , H_2O . The simplified reaction of ferrite formation can presented in the following way:



2.3. Characterization techniques

2.3.1. XRD

Phase composition and structure of the obtained materials were analysed by XRD method with a powder diffractometer with $\lambda_{\text{K}\alpha 1} =$

0.154 nm. The average size of crystallites was calculated by Scherrer's formula: $\langle D \rangle = \frac{0.9\lambda}{\beta_{(311)} \cos \theta}$, where $\beta_{(311)}$ is the full width at half maximum of the (311) reflection, θ is the Bragg angle of the corresponding reflection.

2.3.2. Mossbauer spectroscopy

Mössbauer spectra were measured with MS-1104Em spectrometer ($^{57}\text{Co}(\text{Cr})$ radioactive source, activity of about 40 mCi) at 293 K and 79 K. Calibration of the isomer shifts was done respectively to α -Fe standard (line width 0.29 mm/s). The spectra analysis and fitting procedure were performed using UnivemMs 701 software.

2.3.3. SEM and EDS

Scanning electron micrographs were obtained on a REMMA-102-02 (JCS SELMI, Ukraine) electron microscope with an operating accelerating voltage of 20 kV. An EDS system was used for the elemental microanalysis of the sample surface. Samples for analysis were loaded onto a brass stage.

2.3.4. TEM

Transmission electron microscopy observations were performed using a FEI Osiris microscope equipped with an X-FEG Schottky field emitter (200 kV). SAED patterns were collected with the aperture of 40 μm diameter. STEM imaging was performed using a High Angle Annular Dark Field (HAADF) detector. The samples were deposited on a holey carbon film supported on a copper grid (Agar Scientific, 400 mesh).

2.3.5. FTIR

Fourier-transform infrared spectroscopy (FTIR) spectra were recorded in ATR mode (Alpha-P spectrometer (Bruker)) with 256 scans in the wave number range from 4000 to 400 cm^{-1} with the step of 2 cm^{-1} .

2.3.6. Adsorption properties

Sorption isotherms were determined using batch-mode experiments. Precise amount of the spinel sorbents was placed in flasks containing 50 cm^3 of Pb(II) solution of known concentration, varying in a wide range (from 5 to 100 mg/dm^3). The flasks were shaken at 25 $^\circ\text{C}$ until attaining equilibrium (24 h). Then aliquots of the solutions were taken and Pb(II) concentration was determined by atomic absorption spectrometry (AAS) using an ICE 3000 Series Thermo Scientific spectrometer. The equilibrium sorption capacity, q_e , was calculated with the formula [63]:

$$q_e = \frac{V \cdot (C_0 - C_e)}{m_s} \quad (2)$$

where C_0 is initial Pb(II) ions concentration in solution, [$\text{mg Pb}/\text{dm}^3$]; C_e is the equilibrium concentration of Pb(II) ions in the solution, [$\text{mg Pb}/\text{dm}^3$]; m_s is mass of the spinel sorbent, [g]; q_e is the equilibrium sorption capacity of the sorbent, [$\text{mg Pb}/\text{g}$]; V = volume of the solution containing of Pb(II) ions, [dm^3]. For data analysis, the Langmuir isotherm was used in the following form [63]:

$$q_e = q_{\max} \frac{K_L \cdot C_e}{1 + K_L \cdot C_e} \quad (3)$$

where K_L is Langmuir constant, [$\text{dm}^3/\text{mg Pb}$], q_{\max} is maximum sorption capacity, [$\text{mg Pb}/\text{g}$]. The parameters of the Langmuir equation were computed using the Levenberg-Marquardt optimization procedure.

2.3.7. Magnetic hyperthermia measurements

Magnetic heating of the ferrite nanoparticles was studied using custom-made induction heater operating at fixed frequency of 100 kHz and regulated power up to 1 kW. The magnetic coil (5 cm in

diameter) consisted of six turns of water-cooled copper pipe. Sample tube with water suspension of $\text{Co}_x\text{Zn}_{1-x}\text{Fe}_2\text{O}_4$ magnetic nanoparticles was placed in magnetic coil. The sample temperature was registered using an infrared remote thermometer. Changes of temperature depending on concentration of magnetic nanoparticles and power of the applied magnetic field provide heating parameters important for magnetic hyperthermia applications. Specific loss power (SLP) per mass unit (W/g) was calculated with the following Eq. [64]:

$$SLP = \frac{C \cdot V_s}{m} \left(\frac{dT}{dt} \right) \left[\frac{\text{W}}{\text{g}} \right] \quad (4)$$

where C is the specific heat capacity of water, dT is the change in temperature in dt time period, V_s is the sample volume, m is the mass of the cobalt-zinc ferrite nanoparticles in the water suspension. A more general parameter is Intrinsic Loss Power (ILP) proposed by M. Kallumadil et al. [65] in order to compare heating efficiency of different devices. The ILP parameter takes into account amplitude H and frequency f of the magnetic field applied [65]:

$$ILP = \frac{SLP}{f \cdot H^2} \left[\frac{\text{nH} \cdot \text{m}^2}{\text{kg}} \right]. \quad (5)$$

3. Results and discussion

3.1. Honey characterization

Chemical composition of honey is quite complex. Honey contains a wide variety of substances: mono- and oligosaccharides, organic acids and their salts, nitrogenous compounds (amino acids, proteins), minerals, vitamins, hormones, enzymes, essential oils and much more [66]. FTIR spectrum of the used sample contains absorption bands in the range 750–3700 cm^{-1} (Figure 1). Typical FTIR spectra are divided on two parts: functional group area (4000–1500 cm^{-1}) and fingerprint area (1500–500 cm^{-1}) [67]. The characteristic absorption bands in functional group area belong to O–H stretching vibrations of water, N–H stretching vibrations of proteins, C–H stretching vibrations from lipids, and C=O stretching vibrations [68]. The peak at 2100 cm^{-1} belongs to vibrations of adsorbed CO_2 molecules onto samples surface. The fingerprint area contains C–H deformation vibrations from lipids, N–H deformation and C–N stretching vibrations, C–O and C–C stretching vibrations, C–H bending from the carbohydrates, C–OH and C–C stretching from the carbohydrates [66,67,69]. All the characteristic absorption bands of honey spectrum are listed in Table 2.

3.2. Samples characterization

The X-ray diffraction patterns of the synthesized cobalt-zinc ferrite magnetic nanoparticles are shown in Fig. 2. The resolved peaks in the corresponding X-ray diffraction patterns, indexed to the (220), (311), (5 1 1), (4 0 0) and (4 4 0) crystal planes (JCPDS 22–1012), confirm formation of a single cubic spinel $Fd\bar{3}m$ phase for all the synthesized cobalt-zinc ferrite samples. The broadened XRD peaks indicate that the synthesized samples consist of particles of nanometer sizes. The average values of the crystallites size were calculated using the Scherrer formula, and are presented in Table 3. The lattice constant a for the cobalt-zinc ferrites is distinctly increased with the Zn content increase, virtually in a linear fashion (Fig. 2b), from 8.389 Å for CoFe_2O_4 to 8.414 Å for ZnFe_2O_4 . This is due to different radii of Co (0.58 Å) and Zn (0.6 Å) cations. The cation distribution was obtained from detailed XRD analysis (see Table 3), and the theoretical lattice parameter was calculated (Fig. 2b). It was found that the a_{exp} value depends mainly on the radius of the tetrahedral cations (see inset in Fig. 2b). Furthermore, regardless the zinc content, the size, d , of the nanocrystallites exhibits very similar values in the range of 14 ± 2 nm (Table 3).

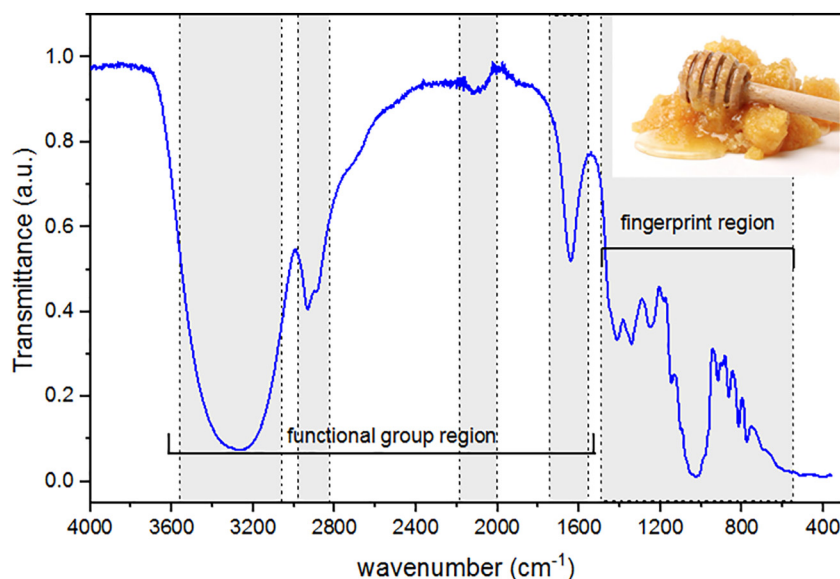


Fig. 1. Fourier-transform infrared spectrum of the floral honey used for Co–Zn ferrite NPs synthesis.

Scanning electron microscopy allowed revealing the nanoparticles size and shape, as well as the degree of their agglomeration. The scanning electron micrographs of cobalt-zinc ferrites are shown in Fig. 3. It

Table 2

Characteristic absorption bands in FTIR spectra of honey used for cobalt-zinc ferrites synthesis.

	wavenumber, cm^{-1}	description
functional group area	3000–3700	O–H stretching vibrations of water
		N–H stretching vibrations of proteins
	2928; 2885	C–H stretching vibrations from lipids
	2100	vibrations of adsorbed CO_2 molecules
fingerprint area	1643	C=O stretching vibrations
	1410	C–H deformation vibrations from lipids
	1339; 1241	N–H deformation and C–N stretching vibrations
	1034	C–O and C–C stretching vibrations
	920	C–H bending from the carbohydrates
	861; 813; 776	C–OH and C–C stretching from the carbohydrates

can be seen that the overall morphology of the examined spinel samples varies not significantly with the Zn content. Marked aggregation of the particles is observed. Its probable cause is the attraction between the magnetic spinel particles, which should decrease with the enhanced Zn content. Despite this effect, the extended agglomeration remains persistent. Porous morphology of the samples is formed due to gaseous

Table 3

Cation distribution of cobalt-zinc ferrites obtained from XRD analysis.

x (Zn^{2+})	a , Å	Cation distribution		d , nm	$\delta = \frac{\text{Fe}^{2+}}{\text{Fe}^{3+}}$
		A-site	B-site		
0.00	8.389	$(\text{Co}_{0.06}^{2+}\text{Fe}_{0.94}^{3+})_A$	$[\text{Co}_{0.94}^{2+}\text{Fe}_{1.06}^{3+}]_B$	12	0.89
0.20	8.393	$(\text{Co}_{0.02}^{2+}\text{Zn}_{0.20}^{2+}\text{Fe}_{0.78}^{3+})_A$	$[\text{Co}_{0.78}^{2+}\text{Fe}_{1.22}^{3+}]_B$	14	0.64
0.40	8.395	$(\text{Co}_{0.05}^{2+}\text{Zn}_{0.40}^{2+}\text{Fe}_{0.55}^{3+})_A$	$[\text{Co}_{0.55}^{2+}\text{Fe}_{1.45}^{3+}]_B$	15	0.38
0.60	8.403	$(\text{Zn}_{0.60}^{2+}\text{Fe}_{0.40}^{3+})_A$	$[\text{Co}_{0.40}^{2+}\text{Fe}_{1.60}^{3+}]_B$	16	0.25
0.80	8.408	$(\text{Zn}_{0.80}^{2+}\text{Fe}_{0.20}^{3+})_A$	$[\text{Co}_{0.20}^{2+}\text{Fe}_{1.80}^{3+}]_B$	13	0.11
1.00	8.414	$(\text{Zn}_{1.00}^{2+})_A$	$[\text{Fe}_{2.00}^{3+}]_B$	14	0.00

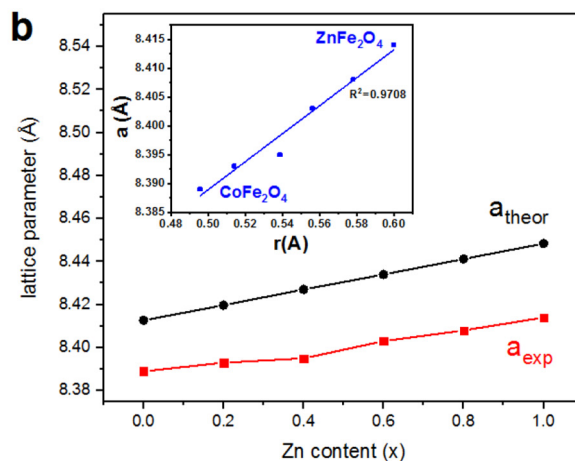
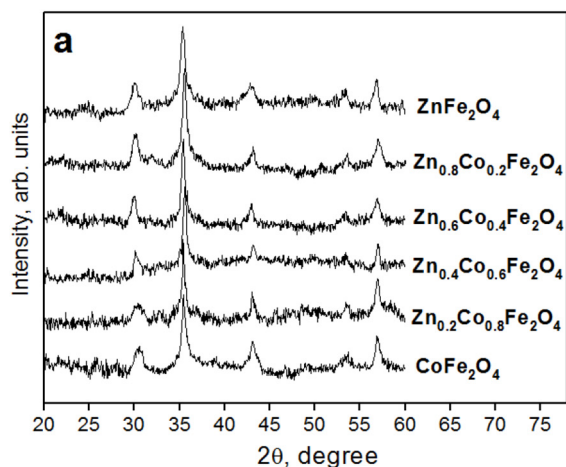


Fig. 2. (a) XRD patterns of the cobalt-zinc ferrite samples; (b) dependence of the spinel lattice parameter of cobalt-zinc ferrites on the Zn content (x). Inset: lattice parameter changes versus average radius of the tetrahedral cations.

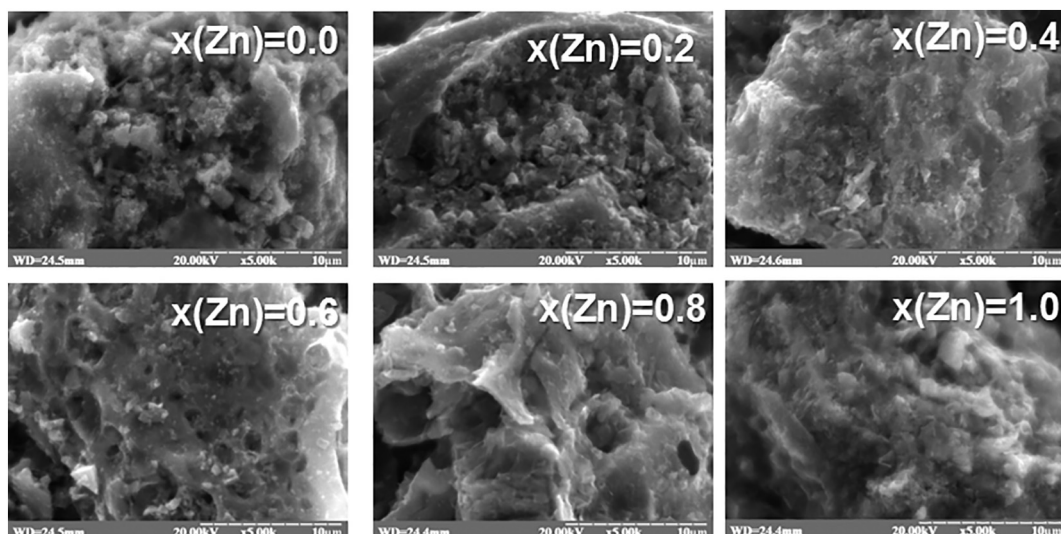


Fig. 3. Scanning electron micrographs of the cobalt-zinc ferrite samples.

products (CO_2 , N_2 , H_2O) released during thermal decomposition of the reagents during the combustion synthesis. This effect is especially visible for the sample with $x(\text{Zn}) = 0.6$. EDS analysis confirmed the presence of chemical elements Co, Zn, Fe and O (Fig. 4). Theoretical and

experimental contents of Co(II) and Zn(II) ions in $\text{Co}_{1-x}\text{Zn}_x\text{Fe}_2\text{O}_4$ samples are compared in Fig. 5a and b. It can be seen that experimental weight contents (%) of all the constituent elements are very close to those theoretically expected.

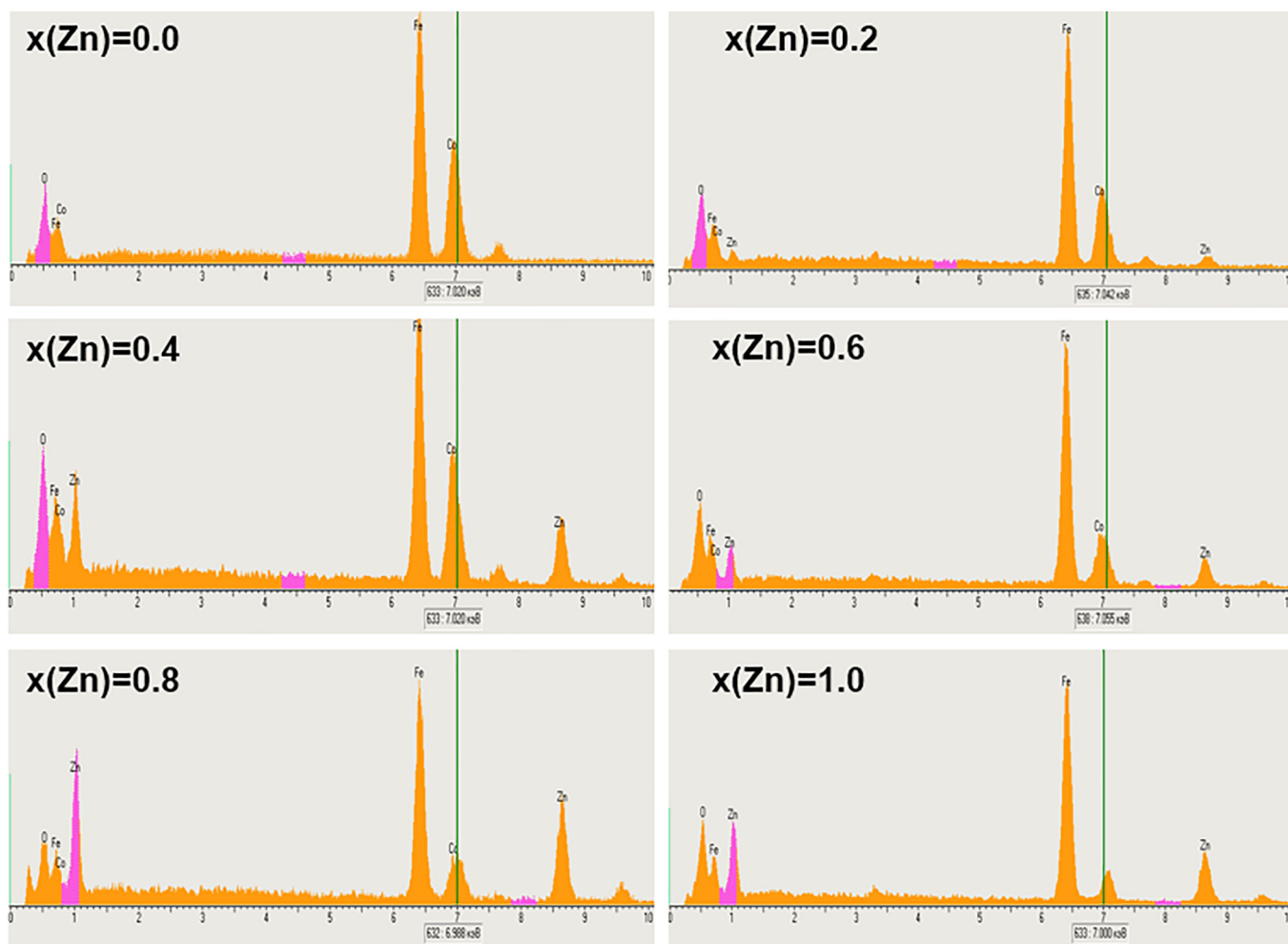


Fig. 4. EDS spectra of the cobalt-zinc ferrite samples.

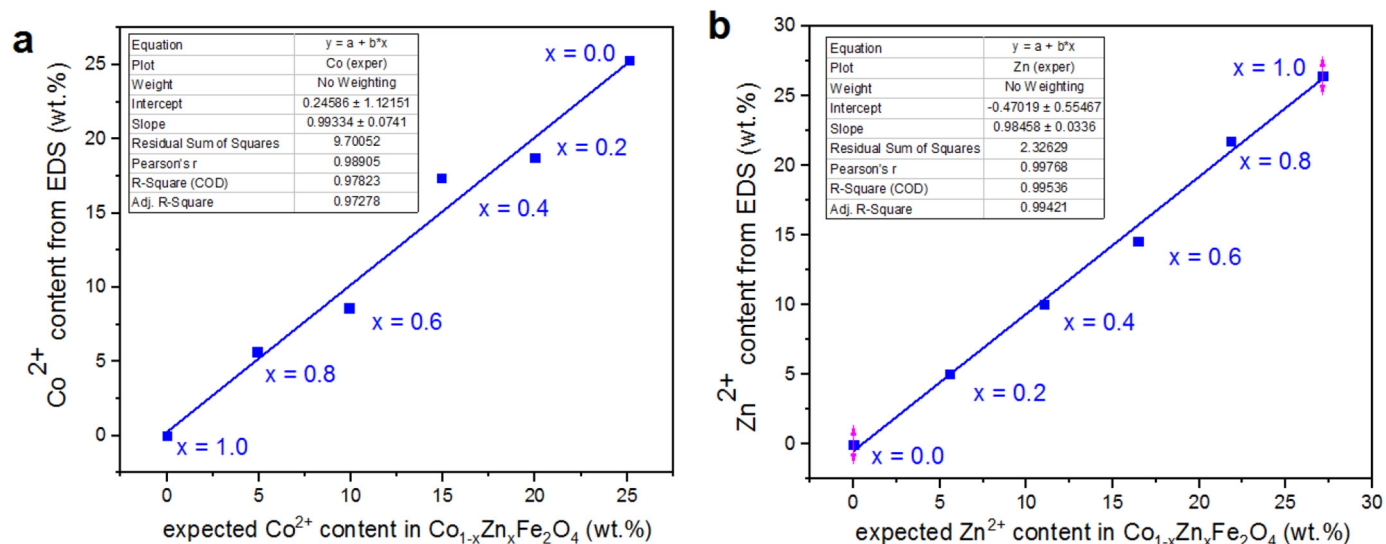


Fig. 5. Parity plots of the EDS and expected content of the (a) Co(II) and (b) Zn(II).

The polyhedral shape and size of the nanoparticles was revealed by TEM (Fig. 6a₁-f₁) and STEM (Fig. 6a₂-f₂) imaging. The corresponding selected area diffraction patterns (SAED), shown in Fig. 6a₃-f₃, confirm the spinel structure of the all samples, and their good crystallinity as well. The particle size distribution (Fig. 6a₄-f₄) exhibits a nearly Gaussian shape for the sample with $\langle d \rangle \geq 30 \pm 2$ nm for $x(\text{Zn}) = 0$, where as with the increasing zinc content it becomes more non-uniform with a tailing towards the higher values. However, the population of the abnormal particles is rather scarce. The latter behavior is most distinct in the case of the sample with $x(\text{Zn}) = 0.4$. Comparison of the size of the nanoparticles determined by TEM with the size of the XRD crystallites, shows that the synthesized cobalt-zinc ferrite nanoparticles are typically composed of 1–4 single crystalline domains, which is consistent with the observed shape of the SAED patterns.

Room temperature Mössbauer spectra of cobalt-zinc ferrites with Zn content of 1.0 and 0.8 mol per formula unit indicate paramagnetic state of these materials (Fig. 7). Weak relaxation character of the Mössbauer spectrum is observed at Zn content equal 0.6 mol per formula unit. The spectrum of the sample with Zn content equal 0.4 mol per formula unit indicates the presence of a magnetically ordered fraction. Decrease of the Zn content down to 0.2 and 0.0 mol per formula unit leads to appearance of a broad sextet with simultaneous decrease of the paramagnetic fraction content. However, the relaxation character of these spectra prevents their detailed analysis.

The registered superparamagnetic properties of the investigated ferrites indicate that single domain state became preferable for ferromagnetic particles with a size less than about 10–20 nm [70]. In this case, the large magnetocrystalline anisotropy, K , causes orientation of the particle magnetization along the easy direction. At the same time, thermal excitation at the condition $k_B T > KV$ (k_B is the Boltzmann constant, T - temperature, V - particle volume) can cause the magnetization flips between two stable orientations, up- and down of the easy direction. Neel relaxation time of the particle magnetic moment τ_N is calculated as $\tau_N = \tau_0 \exp\left(\frac{KV}{k_B T}\right)$, where τ_0 is characteristic relaxation time of the material studied. Values of relaxation time of spinel materials usually fall into range from 10^{-9} to 10^{-11} s. Such flipping leads to zero average magnetization, and to the paramagnetic properties observed.

The observation of superparamagnetic transition depends on the parameters of the experimental technique. The used Mössbauer setup can observe transition for particles with the Neel relaxation time less than the lifetime of the ^{57}Fe nucleus excited state ($\tau_m = 141.8$ ns). Registration of the spectra at low temperatures allows to freeze the magnetization flips, and to obtain information about distribution of the Fe^{3+} ions

between the tetra- and octahedral sublattice sites of spinel structure. The low temperature Mössbauer spectra of the samples with Zn content ≤ 0.6 mol per formula unit demonstrate full transition to magnetically ordered (MO) state for all particles. On the other hand, the samples with the low content of Co ions (0.0 and 0.2) exhibit the effect of superparamagnetic relaxation. The Mössbauer spectra measured at $T = 90\text{K}$ for the samples with the zinc content of $x \leq 0.6$ were well fitted by superposition of three six-line magnetic sub-spectra. Association with the tetrahedrally (A) and octahedrally (B) coordinated Fe^{3+} was performed according to the isomeric shift values (Table 4). The isomeric shift for the iron ions located in the A-sites is typically smaller, as a result of stronger covalence of the $\text{Fe}_A\text{-O}$ bonds. The calculated parameters of the Mössbauer spectra are presented in Table 4.

The values of the size of superparamagnetic particles were computed as well. The size of the superparamagnetic particles, equal to 14 ± 2 nm is very close to the average XRD size of the single crystallites, for all synthesized samples. In this case, the magneto-crystalline anisotropy K is the main parameter, which determines the conditions of the superparamagnetic (SP) transition for the investigated ferrite particles. The high-spin Co^{2+} ions ($S = 3/2$) located in the octahedral sites contribute to the orbital magnetic moment, and cause an increase of the magneto-crystalline anisotropy. So, transition from the superparamagnetic state to the magnetically ordered one was observed at respectively lower size of the particles. One more important parameter is characteristic time of magnetic moment oscillations, τ_0 . This parameter is size-sensitive, and is decreased exponentially from $16.7 \cdot 10^{-10}$ s to $3.8 \cdot 10^{-10}$ s for CoFe_2O_4 nanoparticles [71] (Fig. 8). Assuming that the composition-induced changes of τ_0 can be neglected for $0.0 \leq x(\text{Zn}) \leq 0.6$, the characteristic τ_0 value for 14 nm ferrite particles is equal to $3.4 \cdot 10^{-10}$ s.

Temperature dependence of the magneto-crystalline anisotropy of the bulk cobalt ferrite in temperature range from 20 K to 350 K is described by the empirical relation $K_T = K_0 \exp(-A/T^2)$, where $K_0 = 1.96 \cdot 10^6$ J/m³ and $A = 1.9 \cdot 10^{-5}$ K² [72]. At the same time, a decrease of the particle sizes causes the corresponding decrease of the magneto-crystalline anisotropy: from $7.5 \cdot 10^5$ J/m³ for the particles about 5 nm in size [73] to $3.1 \cdot 10^5$ J/m³ for the particles of about 10–15 nm in size [74]. The zinc ions do not exhibit angular magnetic momentum, and therefore, do not contribute to the magneto-crystalline anisotropy values. So, an increase of the Zn content leads to fast decrease of the K values. The value of the magneto-crystalline anisotropy of the sample with $x(\text{Zn}) = 1.0$ (which is close to the paramagnetic state) was calculated to be approximately $5.2 \cdot 10^3$ J/m³.

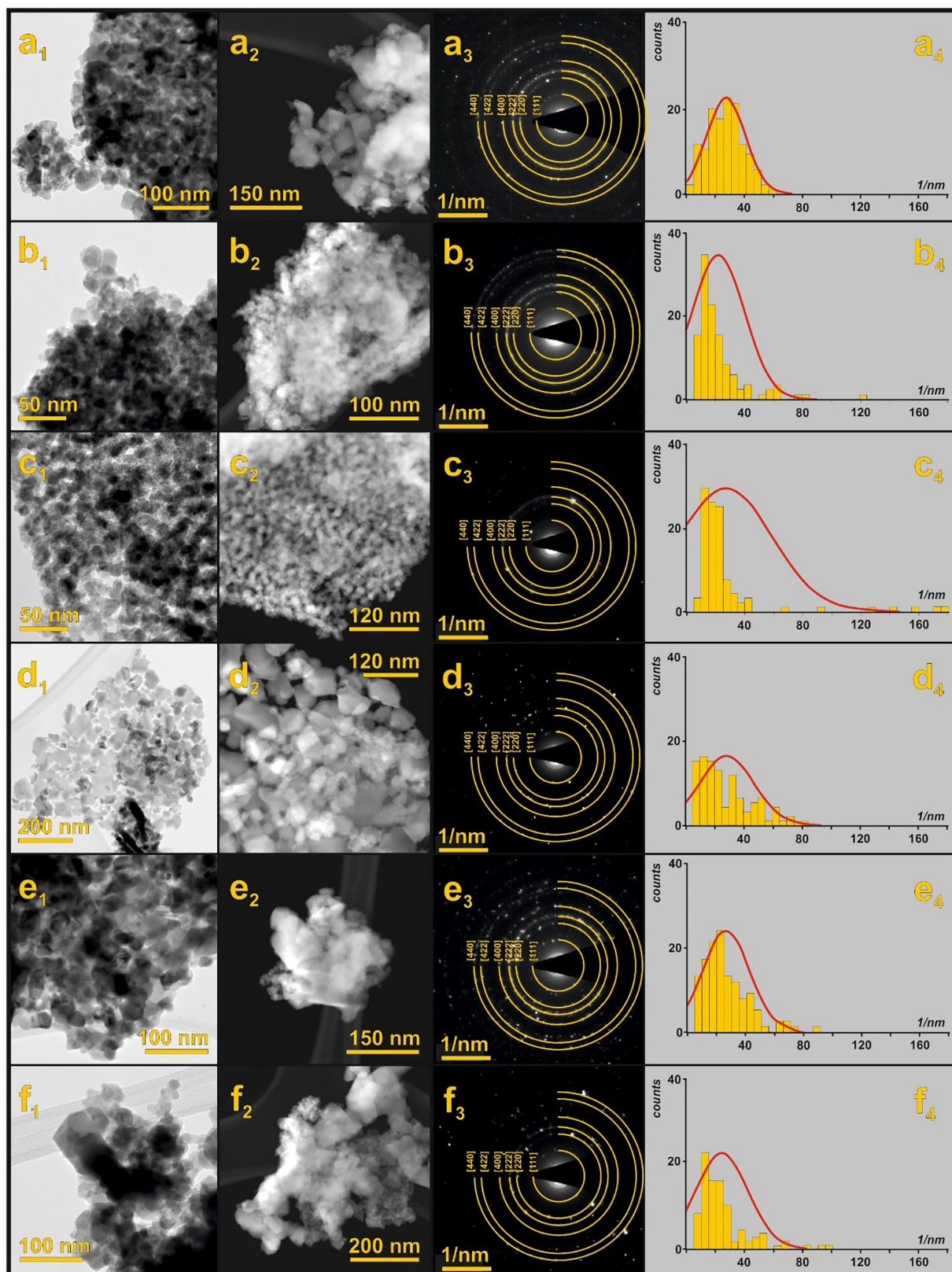


Fig. 6. TEM (a₁ - f₁), STEM (a₂ - f₂), SAED patterns (a₃ - f₃) and the nanoparticle size distribution of the cobalt-zinc ferrite samples with $x(\text{Zn}) = 0$ (a), $x(\text{Zn}) = 0.2$ (b), $x(\text{Zn}) = 0.4$ (c), $x(\text{Zn}) = 0.6$ (d), $x(\text{Zn}) = 0.8$ (e) and $x(\text{Zn}) = 1$ (f).

Zinc-cobalt mixed ferrite can be represented as $(\text{Zn}_x\text{Co}_y^{2+}\text{Fe}_{1-x-y}^{3+})_A[\text{Co}_z^{2+}\text{Fe}_{2-z}^{3+}]_B\text{O}_4$, where z stands for the inversion degree. Distribution of the Fe^{3+} ions between the tetrahedral (A) and octahedral (B) coordination sites was calculated using both the Mössbauer and

EDS data (Table 5). The experimental EDS values of the Co/Fe and Zn/Fe molar ratios were marked as K_1 and K_2 respectively. The Mössbauer analysis allows also to calculate the ratio of Fe^{3+} ions in the tetrahedral and octahedral interstitials of the spinel lattice

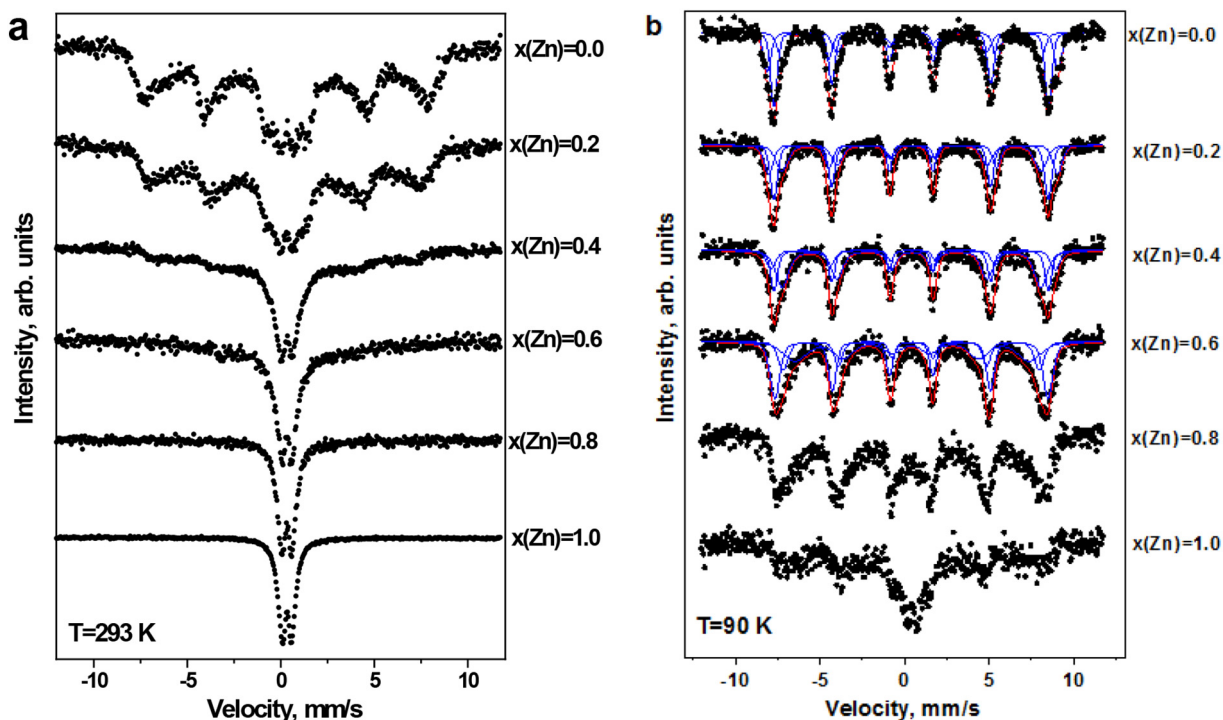


Fig. 7. Mössbauer spectra of the synthesized cobalt-zinc ferrites, measured at (a) 293 K and (b) 90 K.

(Fe_A/Fe_B), which was labeled as K₃ (Table 5). The molar ratios were presented in a form of three equations: $(y + z)/(3 - x - y - z) = K_1$; $x/(3 - x - y - z) = K_2$; $(1 - x - y)/(2 - z) = K_3$. This set of the equations was solved for all the studied samples, and the obtained results are presented in Table 5. The calculated cation distributions for Co_{1-x}Zn_xFe₂O₄ (0 ≤ x ≤ 1) ferrites are described in Table 6. It can be concluded that the cation distribution obtained from the Mössbauer analysis is quite close to the cation distribution obtained from the XRD data.

The FTIR spectra of the examined ferrite samples are shown in Fig. 9. The observed characteristic peaks are ascribed to vibrations of the metal-oxygen bonds and to the vibrations of the functional groups of the honey components. The strong peaks at the wave numbers 450–500 cm⁻¹ (ν₁) and 620–630 cm⁻¹ (ν₂) correspond to the vibrations of the M-O bonds in octahedral and tetrahedral sites,

respectively (Table 7). With zinc content increase, the position of the ν₁ peak is shifted towards long-wavelength region. Low-intensity bands in the range 1000–2000 cm⁻¹ refer to the vibrations of the N-H, C-H, C=O bonds of the organic residues of the parent honey, whereas the strong broad peak at 3500 cm⁻¹ corresponds to the vibrations of water molecules. The obtained spectra correspond well to the literature data [75]. The observed characteristic bands differ only in the peak intensity. Thus, one can infer that some minor honey residues are present on surface of the ferrite nanoparticles. The obtained data reveal possible application of the studied magnetic NPs in biomedical applications.

The frequencies of the metal-oxygen bond stretching peaks enable to calculate the corresponding bond force constants [76]:

$$k_T = 7.62 \cdot M_1 \cdot \nu_1^2 \cdot 10^{-3} \text{ (dyne/cm}^2\text{)} \quad (6)$$

$$k_O = 10.62 \cdot \frac{M_2}{2} \cdot \nu_2^2 \cdot 10^{-3} \text{ (dyne/cm}^2\text{)} \quad (7)$$

Table 4

The parameters of the Mössbauer spectra of cobalt-zinc ferrites measured at 90 K (*I_s* is isomer shift; *Q_s* is quadrupole splitting; *H* is hyperfine field; *S* is relative integral intensity; *G* is line width).

	Site	<i>I_s</i> /mm·s ⁻¹	<i>Q_s</i> /mm·s ⁻¹	<i>H</i> ,/kOe	<i>S</i> /%	<i>G</i> ,/mm·s ⁻¹
(Co _{0.94} ²⁺ Fe _{0.06} ³⁺) _A (Co _{0.94} ²⁺ Fe _{1.06} ³⁺) _B O ₄ (CoFe ₂ O ₄)						
1	A1	0.39	-0.002	503.8	46.8	0.47
2	B1	0.48	0.003	533.6	27.6	0.53
3	B2	0.41	-0.032	471.5	25.6	0.67
(Zn _{0.18} ²⁺ Co _{0.82} ²⁺ Fe _{0.80} ³⁺) _A (Co _{0.78} ²⁺ Fe _{1.22} ³⁺) _B O ₄ (Zn _{0.2} Co _{0.8} Fe ₂ O ₄)						
1	A1	0.39	0.001	503.4	40.3	0.51
2	B1	0.49	0.013	529.7	27.1	0.64
3	B2	0.42	-0.051	474.7	32.6	0.87
(Zn _{0.36} ²⁺ Co _{0.64} ²⁺ Fe _{0.59} ³⁺) _A (Co _{0.59} ²⁺ Fe _{1.41} ³⁺) _B O ₄ (Zn _{0.4} Co _{0.6} Fe ₂ O ₄)						
1	A1	0.40	-0.003	503.6	29.5	0.48
2	B1	0.50	0.012	521.4	19.2	0.66
3	B2	0.43	-0.028	474.7	51.3	0.93
(Zn _{0.56} ²⁺ Co _{0.44} ²⁺ Fe _{0.44} ³⁺) _A (Co _{0.38} ²⁺ Fe _{1.62} ³⁺) _B O ₄ (Zn _{0.6} Co _{0.4} Fe ₂ O ₄)						
1	A1	0.40	-0.08	470.2	21.7	0.70
2	B1	0.43	0.007	500.8	43.3	0.68
3	B2	0.41	0.067	429.9	35.0	1.66

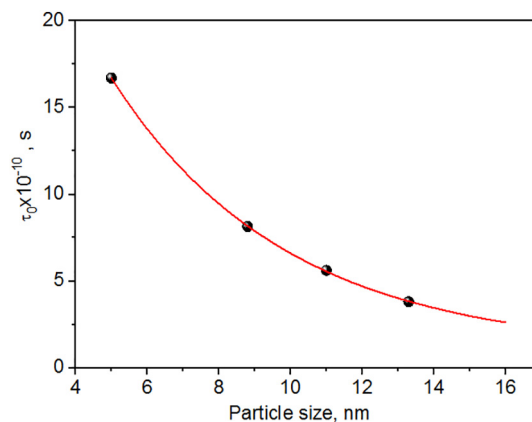


Fig. 8. The dependency of characteristic time τ₀ of the magnetic moment oscillations for CoFe₂O₄ nanoparticles (calculated using the data presented in [71]).

Table 5Theoretical and experimental (EDS and Mössbauer spectroscopy) results for the Zn²⁺, Co²⁺ and Fe³⁺ ions content in the synthesized Co–Zn ferrites.

Co ²⁺ molar content (predicted)	Chemical composition										
	Theoretical					Experimental					
	Co, wt%	Zn, wt%	Fe, wt%	Co/Fe, molar ratio	Zn/Fe, molar ratio	Co, wt%	Zn, wt%	Fe, wt%	Co/Fe, molar ratio (K ₁)	Zn/Fe, molar ratio (K ₂)	Fe _T /Fe _O , molar ratio (K ₃)
1	25.12	0	47.6	0.50	0.00	25.32	0	47.42	0.50	0.00	0.89
0.8	19.98	5.55	47.34	0.40	0.10	19.77	5.05	48.86	0.38	0.09	0.66
0.6	14.91	11.03	47.08	0.30	0.20	15.4	10.04	45.73	0.32	0.19	0.42
0.4	9.88	16.45	46.83	0.20	0.30	9.63	15.57	49.59	0.18	0.27	0.28
0.2	4.92	21.82	46.58	0.10	0.40	5.67	21.77	45.95	0.12	0.40	–
0	0	27.13	46.33	0.00	0.50	0	26.47	46.9	0.00	0.48	–

where k_T and k_O are bond force constants of tetrahedral and octahedral sites, respectively; M_1 and M_2 are atomic masses of the respective cations in the tetrahedral and octahedral sites. The obtained values are listed in Table 7. The bond force constants are known to be inversely related with the corresponding bond lengths. The transition from cobalt ferrite to zinc ferrite is accompanied by substitution of the relevant cations in the both tetrahedral and octahedral sublattices of the spinel cell. The zinc ions ($r(\text{Zn}^{2+})_A = 0.6 \text{ \AA}$) are larger in size than the cobalt ions ($r(\text{Co}^{2+})_A = 0.58 \text{ \AA}$) and the ferric ions ($r(\text{Fe}^{3+}) = 0.49 \text{ \AA}$). Thus, replacement of the Co ions by the Zn ones leads to an increase of the tetrahedral bond length and to decrease of the octahedral bond length. In such case, the values of the force constants should be inversely proportional. Fig. 10 supports this statement as the tetrahedral force constant k_T decreases and octahedral force constant k_O increases with the increasing Zn content.

Debye temperature, θ_D , is related with many properties of solids, such as specific heat, electrical conductivity, thermal conductivity and

elastic properties, and can be estimated using the following formula [77]:

$$\theta_D = \frac{h \cdot c \cdot \nu_{\text{avg}}}{k_B} \quad (8)$$

where h is Planck constant ($h = 662,606,957 \times 10^{-34} \text{ J}\cdot\text{s}$); c is light velocity ($c = 3 \times 10^{10} \text{ cm/s}$); $\nu_{\text{avg}} = \frac{(\nu_1 + \nu_2)}{2}$ (ν_1 and ν_2 are peak frequencies of the M–O bonds of the octahedral and tetrahedral sites, respectively). The calculated values of Debye temperature are varying between 782 and 805 K (Table 7). Fig. 11 shows dependence of the Debye temperature on the Zn content. It can be seen that θ_D increases with increase of the Zn molar fraction above 0.6.

Fig. 12 reveals a clear linear relationship between the octahedral force constant and the Debye temperature. It is known that excitation of the bond vibration modes depends on the Debye temperature. The

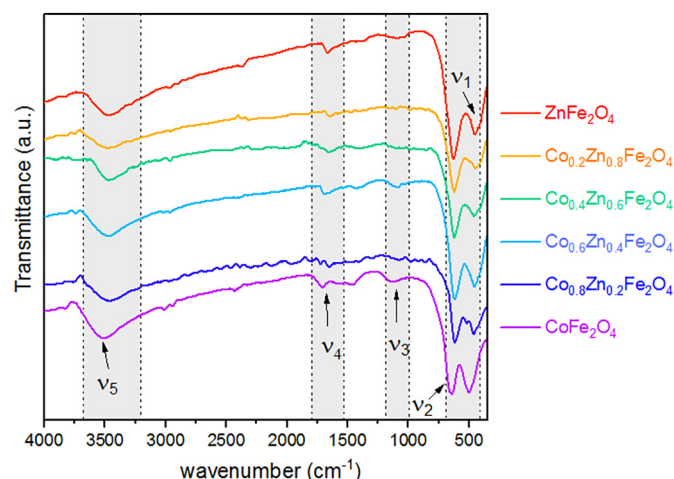
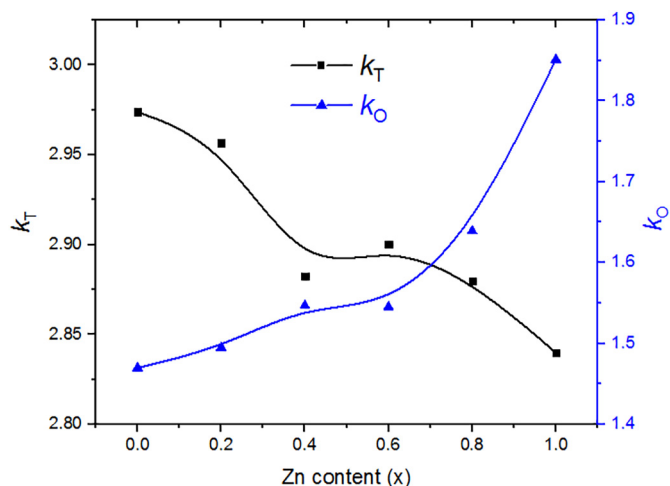
Table 6The calculated cation distributions for Zn_xCo_{1-x}Fe₂O₄ (0 ≤ x ≤ 1) ferrites.

Theoretical Zn ²⁺ content	Experimental cation distribution
0.00	(Co _{0.06} ²⁺ Fe _{0.94} ³⁺) _A (Co _{0.94} ²⁺ Fe _{1.06} ³⁺) _B O ₄
0.20	(Zn _{0.18} ²⁺ Co _{0.82} ²⁺ Fe _{0.50} ³⁺) _A (Co _{0.78} ²⁺ Fe _{1.22} ³⁺) _B O ₄
0.40	(Zn _{0.36} ²⁺ Co _{0.64} ²⁺ Fe _{0.59} ³⁺) _A (Co _{0.59} ²⁺ Fe _{1.41} ³⁺) _B O ₄
0.60	(Zn _{0.56} ²⁺ Co _{0.44} ²⁺ Fe _{0.44} ³⁺) _A (Co _{0.38} ²⁺ Fe _{1.62} ³⁺) _B O ₄
0.80*	(Zn _{0.79} ²⁺ Fe _{0.21} ³⁺) _A (Co _{0.21} ²⁺ Fe _{1.79} ³⁺) _B O ₄
1.00*	(Zn _{0.97} ²⁺ Fe _{0.03} ³⁺) _A (Fe _{3.00} ³⁺) _B O ₄

* the calculation of the cation distribution for the samples with Zn²⁺ theoretical content 1.00 and 0.80 was performed using the EDS data only.

Table 7Wavenumbers of the IR absorption bands, bond force constants (k_T and k_O) and ($\nu_1 - \nu_2$) differences for the cobalt-zinc ferrite samples.

Zn ²⁺ (x)	ν_1 (cm ⁻¹) (B-site)	ν_2 (cm ⁻¹) (A-site)	$k_T \times 10^6$ (dyn/cm ²)	$k_O \times 10^6$ (dyn/cm ²)	k (avg)	$\nu_1 - \nu_2$ (K)	θ_D (K)
0	448.0	638.0	2.974	1.470	2.222	190.0	782.2
0.2	452.0	634.0	2.957	1.495	2.226	182.0	782.2
0.4	460.0	624.0	2.883	1.547	2.215	164.0	780.7
0.6	460.0	624.0	2.900	1.545	2.223	164.0	780.7
0.8	474.0	620.0	2.880	1.639	2.259	146.0	787.9
1	504.0	614.0	2.840	1.851	2.346	110.0	805.2

**Fig. 9.** FTIR spectra of the cobalt-zinc ferrite samples.**Fig. 10.** Dependence of the tetrahedral force constant k_T and the octahedral force constant k_O on the Zn content (x) in the samples.

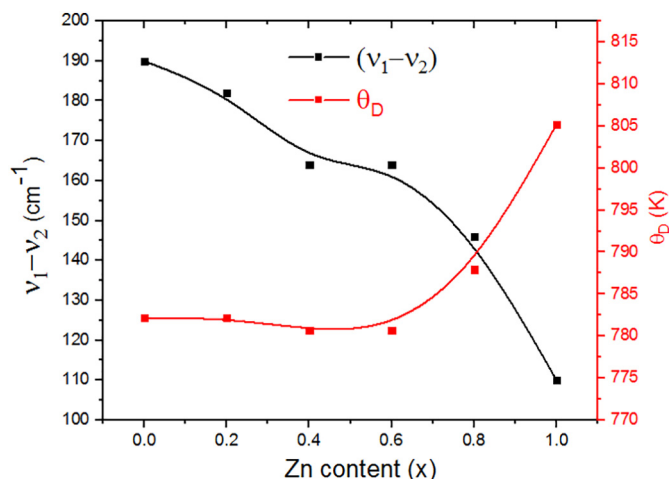


Fig. 11. Dependence of Debye temperature and difference in wavenumber frequencies on zinc content in Co–Zn ferrites.

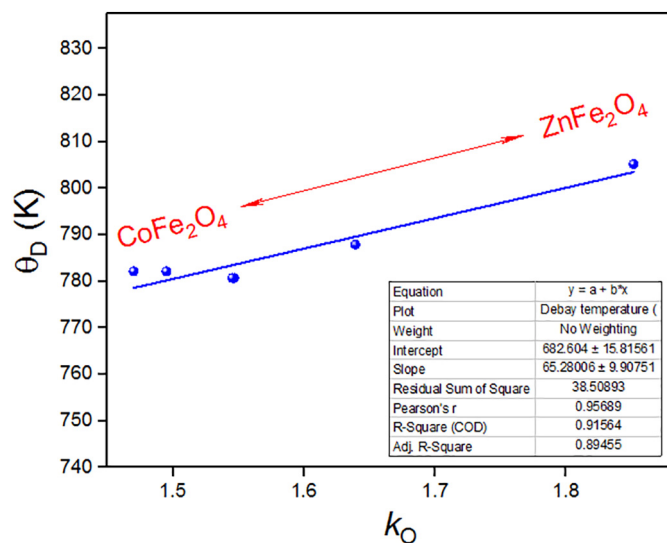


Fig. 12. Relationship between octahedral bond force constant k_O and Debye temperature for Co–Zn ferrite samples.

observed variation of the Debye temperature with composition may be interpreted in terms of the bond forces changes in the spinel lattice. Crystals with strong interatomic interactions are characterized by a high value of θ_D . The observed increase in Debye temperature (θ_D) with the increasing zinc content (x) suggests that the metal-oxygen bond vibrations are hampered upon replacement of the Co ions by Zn ones. In other words, the strength of the interatomic bonds is increased with increasing content of zinc (x). Indeed, when the large cobalt ions are replaced by the smaller ferric ions in the octahedral sublattice, the resultant decrease in the bond length leads to the corresponding increase in the bond strength.

3.3. Adsorption of Pb^{2+} ions

Environmental issues motivate researchers to develop efficient sorbents that are convenient in use and are easily separable [63,78–81]. Therefore, the obtained magnetic cobalt-zinc ferrites were examined as sorbents of lead ions in aqueous media (Fig. 13). It is seen that $CoFe_2O_4$ has the lowest adsorption capacity equal to 16 mg/g. Adsorption capacity of the Zn-substituted samples is increased from 23 mg/g (for $Co_{0.8}Zn_{0.2}Fe_2O_4$) to 289 mg/g (for $ZnFe_2O_4$). Therefore, the four

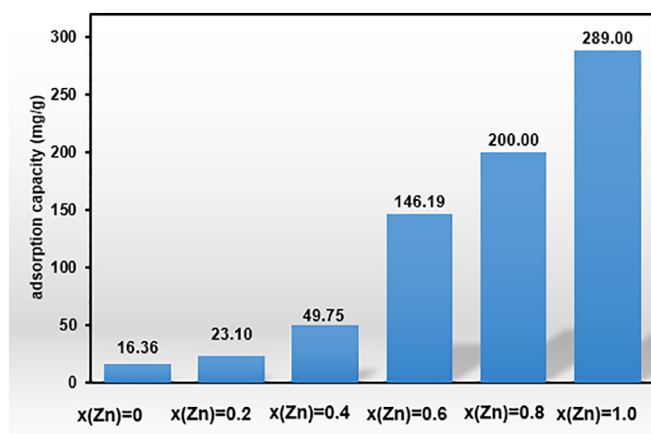


Fig. 13. Lead (Pb^{2+}) adsorption capacity of cobalt-zinc ferrites depending on zinc molar content. (Experimental conditions: initial concentration of Pb^{2+} ions = 17 mg/L; volume of Pb^{2+} solution = 50 ml; mass of the adsorbent = 2 mg; agitation time = 24 h; pH = 7).

most promising samples, with $x(Zn) = 0.4, 0.6, 0.8$ and 1.0 , were selected for further detailed adsorption experiments.

Adsorption experiments were carried out in batch mode using model solutions of Pb^{2+} ions and magnetic cobalt-zinc ferrites. Adsorption isotherms are depicted in Fig. 14a. The values of the sorption capacity are clearly increased with increase of Zn content in cobalt-zinc ferrites. The adsorption capacity of sample with $x(Zn) = 0.4$ is equal to 65.5 mg/g, while the adsorption capacity of the sample with $x(Zn) = 1.0$ is four times higher, and equal to 270.3 mg/g. The Langmuir, Freundlich and Dubinin-Radushkevich models were used for analyzing the adsorption mechanism (Fig. 14b–c). According to the Langmuir model, each surface-active center attracts one Pb^{2+} cation and a monomolecular layer is formed. Linear form of the Langmuir isotherm is described by the eq. 9 [82]:

$$\frac{C_e}{q_e} = \left(\frac{1}{q_{max}} \right) C_e + \frac{1}{q_{max} K_L} \quad (9)$$

where q_e (mg/g) is adsorption capacity; q_{max} (mg/g) is the maximum adsorption capacity; C_e (mg/L) is the Pb^{2+} equilibrium concentration; K_L (L/mg) is a Langmuir constant. Thus, a plot of C_e/q_e vs. C_e (Fig. 12b) gives values of q_m and K_L (Table 8). A separation factor R_L has been calculated using the formula (10) [82]:

$$R_L = \frac{1}{1 + K_L C_o} \quad (10)$$

where K_L (L/mg) is Langmuir constant; C_o (mg/L) is initial Pb^{2+} concentration. The separation factor R_L provides information about the sorption character: linear ($R_L = 1$), unfavorable ($R_L > 1$), favorable ($0 < R_L < 1$), or irreversible ($R_L = 0$). The obtained values (Table 8) are in the range $0 < R_L < 1$ indicating clearly that surface of cobalt-zinc ferrites is favorable for sorption of the Pb^{2+} ions. With increase of zinc content in the sorbent materials, the values of the maximal capacity q_{max} and the coefficient K_L are increased. In other words, both the sorption capacity and the sorbent affinity are increased. The quite large value of $K_L = 2.272$ for the sample with $x(Zn) = 1.0$ indicates a strong interaction between the Pb^{2+} ions and the ferrite surface.

An alternative Freundlich model of the adsorption data treatment takes into account a probable multilayer adsorption. The linear form of Freundlich equation may be presented as the following [82]:

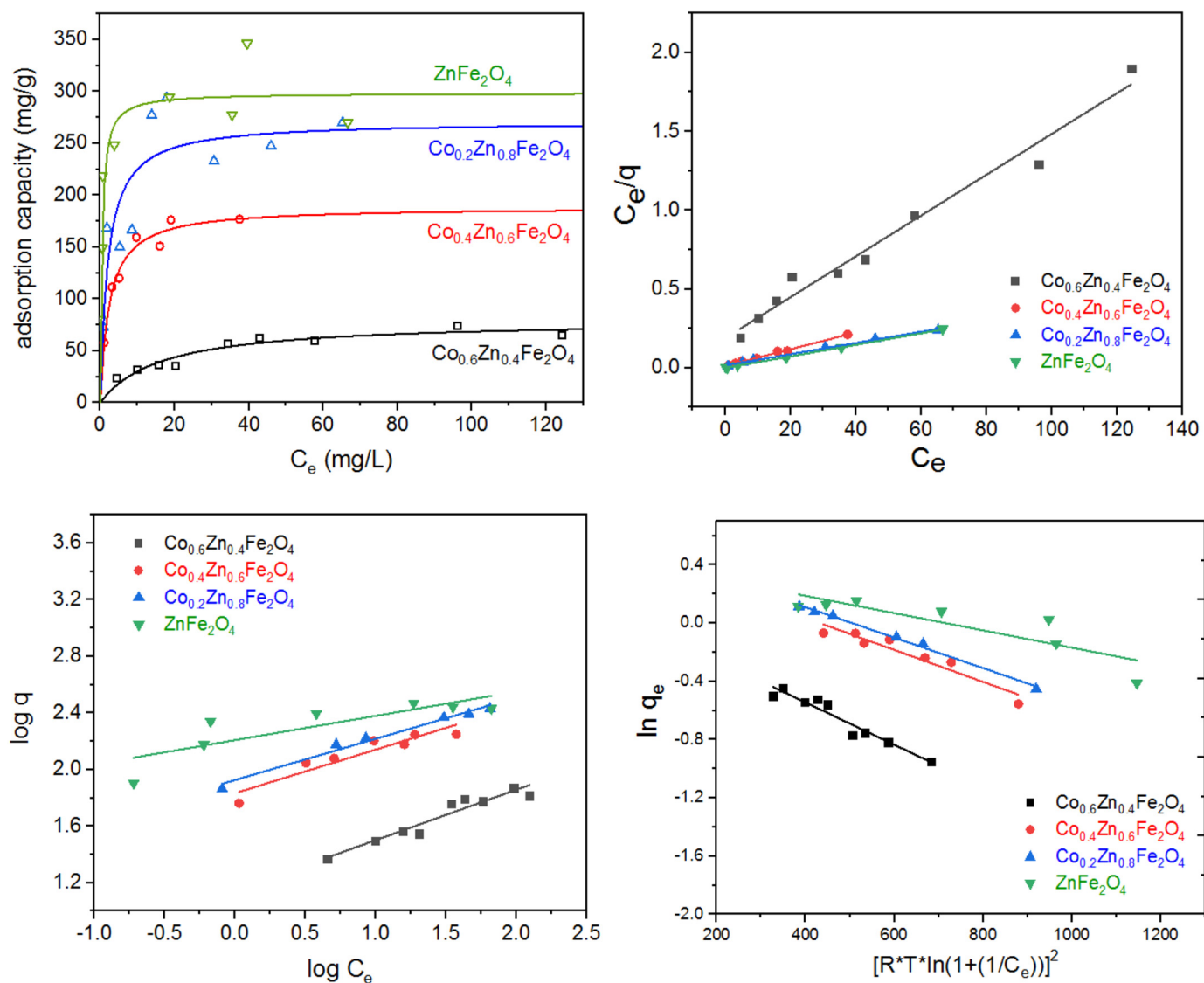


Fig. 14. Sorption isotherms (a) and transformations according to the Langmuir (b), Freundlich (c) and Dubinin–Radushkevich (d) models. C_e is equilibrium concentration.

$$\log q_e = n \log C_e + \log K_F \tag{11}$$

where q_e (mg/g) is equilibrium adsorption; C_e (mg/L) is equilibrium concentration of the Pb^{2+} ions, K_F (mg/g)/(mg/L)ⁿ is the Freundlich constant; n is a parameter indicating adsorption intensity. The value of n is usually interpreted in terms of the surface heterogeneity. The linear plot of $\log q_e$ vs. $\log C_e$ (Fig. 14c) gives the Freundlich constant K_F and parameter n . Adsorption is favorable when $n > 1$. The calculated values of the Freundlich constants are presented in Table 1. All the values of parameter n are larger than 1. Thus, adsorption of Pb^{2+} ions on the studied

magnetic spinel sorbents is clearly favorable. The values of the Freundlich constant, K_F , for Pb^{2+} adsorption increase with the increasing Zn content: $K_F = 13.9$ ($x(\text{Zn}) = 0.4$) < $K_F = 68.1$ ($x(\text{Zn}) = 0.6$) < $K_F = 84.4$ ($x(\text{Zn}) = 0.8$) < $K_F = 161.4$ ($x(\text{Zn}) = 1.0$). This regularity confirms the highest adsorption activity of the $ZnFe_2O_4$ sample. The highest values of the correlation coefficient are observed in the case of the Langmuir model. This fact implies that Pb^{2+} ions are adsorbed on ferrite nanoparticles in the monolayer fashion.

The Dubinin–Radushkevich model, in turn, was involved in order to distinguish between physical and chemical adsorption (Fig. 14d). This model is described by the eq. (12) [82]:

Table 8
The isotherm parameters for the Pb^{2+} adsorption.

Sample	Langmuir model				Freundlich model			D-R model			
	q_{max}	K_L	R_L	R^2	n	K_F	R^2	β	q_{max}	E	R^2
$x(\text{Zn}) = 0.4$	79.92	0.061	0.11–0.75	0.976	2.8	13.9	0.921	0.0015	214.9	18.26	0.929
$x(\text{Zn}) = 0.6$	188.70	0.414	0.05–0.42	0.996	3.3	68.1	0.883	0.0011	333.1	21.32	0.912
$x(\text{Zn}) = 0.8$	271.21	0.489	0.06–0.34	0.995	3.4	84.4	0.981	0.0010	351.9	22.36	0.994
$x(\text{Zn}) = 1.0$	298.71	2.272	0.01–0.10	0.999	5.8	161.4	0.691	0.0006	317.1	28.87	0.929

$$\ln q_e = -K_{DR}\varepsilon^2 + \ln q_{DR} \quad (12)$$

where q_{DR} (mg/g) is theoretical adsorption capacity; K_{DR} (mol^2/kJ^2) is a D-R constant; ε is Polanyi adsorption potential. The K_{DR} constant gives the value of the mean adsorption energy E (kJ/mol), with using Eq. (13) [82]:

$$E = \frac{1}{\sqrt{2K_{DR}}} \quad (13)$$

If $E < 16$ kJ/mol, adsorption occurs along a physical mechanism, and if $E > 16$ kJ/mol, adsorption occurs along a chemical mechanism. As can be seen in Table 3, the values of the adsorption energy are higher than 16 kJ/mol. Thus, mechanism of the Pb^{2+} adsorption is the chemisorption one.

Adsorption activity of the examined cobalt-zinc ferrites can be linked with the surface acid-base properties of the samples. The ionic-covalent parameter (ICP) was used for evaluation of the acid-base properties of $\text{Co}_{1-x}\text{Zn}_x\text{Fe}_2\text{O}_4$ surface [83]. The ICP parameter takes into account cation distribution and ionic radii of the cations in the tetrahedral and octahedral sites depending on their coordination number [84]. The values of Σ ICP for $\text{Co}_{1-x}\text{Zn}_x\text{Fe}_2\text{O}_4$ spinels were calculated by the following formula (14) [83]:

$$\begin{aligned} \Sigma \text{ ICP} = & c(\text{Zn}_A^{2+}) \cdot \text{ICP}(\text{Zn}_A^{2+}) + c(\text{Co}_A^{2+}) \cdot \text{ICP}(\text{Co}_A^{2+}) \\ & + c(\text{Fe}_A^{3+}) \cdot \text{ICP}(\text{Fe}_A^{3+}) + c(\text{Co}_B^{2+}) \cdot \text{ICP}(\text{Co}_B^{2+}) \\ & + c(\text{Fe}_B^{3+}) \cdot \text{ICP}(\text{Fe}_B^{3+}) \end{aligned} \quad (14)$$

where c is the concentration of the cations and ICP is the partial ionic-covalent parameter for the A- and B-sites. The values of the partial ICP were calculated using the eq. (15) [83]:

$$\text{ICP} = \log P - 1.38\chi + 2.07 \quad (15)$$

where P is polarizing power of the cation, calculated as $P = Z/r^2$ (Z is formal cation charge and r is Shannon ionic radius [85]); χ is electronegativity of the given cation ($\chi(\text{Co}^{2+}) = 1.467$; $\chi(\text{Zn}^{2+}) = 1.428$; $\chi(\text{Fe}^{3+}) = 1.687$) [86]. An increase in the zinc content causes the resultant increase of the Σ ICP value, indicating enhancement of the acidic properties of the $\text{Co}_{1-x}\text{Zn}_x\text{Fe}_2\text{O}_4$ surface. The dependence of the adsorption capacity of the Co-Zn ferrites on the ionic-covalent parameter is

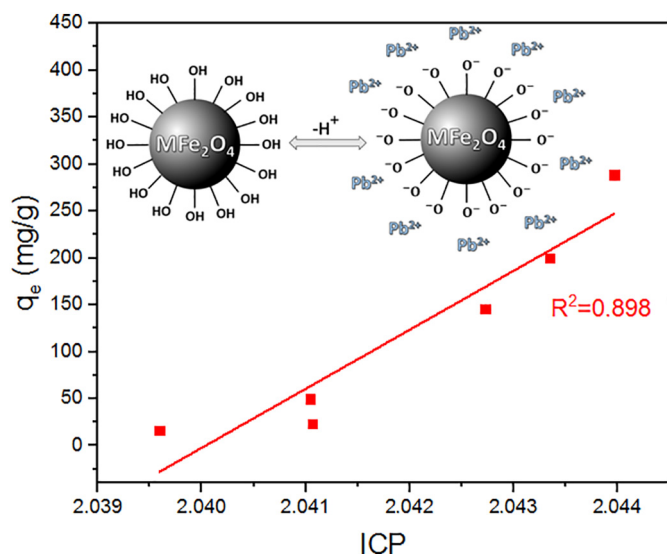


Fig. 15. Adsorption capacity of Co–Zn ferrites versus the ionic-covalent parameter of the spinel.

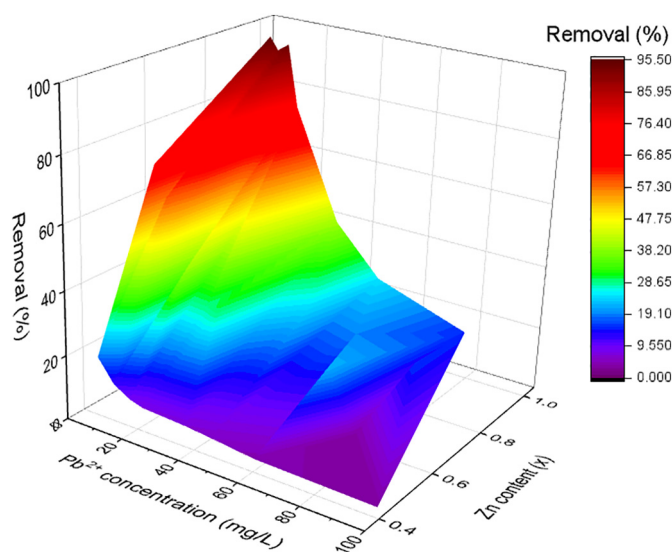


Fig. 16. Removal efficiency of Pb^{2+} ions from aqueous solutions with cobalt-zinc ferrites.

Table 9

Adsorption capacity of the studied adsorbents towards Pb^{2+} ions.

Adsorbent	q_{max} (mg/g)	Ref.
iron-trimesic metal-organic frameworks	3.56	[90]
CuFe_2O_4	4.50	[91]
NiFe_2O_4	41.50	[54]
CoFe_2O_4	44.20	[54]
graphene oxide/ NiFe_2O_4	46.03	[51]
ZnFe_2O_4	47.10	[54]
hydrochar/MgAl-layered double hydroxides composites	62.40	[92]
Mn–Zn ferrite/biochar composite	99.50	[93]
zinc ferrite-alginate beads	108.80	[56]
MgFe_2O_4 /graphene oxide	143.0	[94]
molybdenite	147.80	[95]
Fe_3O_4 -decorated porous BN nanofibers	203.75	[96]
Fe_3O_4 @TATS@ATA	205.20	[97]
$\text{Co}_{0.6}\text{Zn}_{0.4}\text{Fe}_2\text{O}_4$	79.92	this study
$\text{Co}_{0.4}\text{Zn}_{0.6}\text{Fe}_2\text{O}_4$	188.70	this study
$\text{Co}_{0.2}\text{Zn}_{0.8}\text{Fe}_2\text{O}_4$	271.21	this study
ZnFe_2O_4	298.71	this study

depicted in Fig. 15. Clearly, the higher is surface acidity the higher is adsorption capacity. Efficiency of the cobalt-zinc ferrites in removal of the Pb^{2+} ions is depicted in Fig. 16, and it can be seen that zinc ferrite is the most effective one. Comparison of the adsorption capacity of the studied adsorbents towards Pb^{2+} ions is presented in Table 9.

3.4. Magnetic hyperthermia measurements

Magnetic nanoparticles (MNPs) are used in the medicine and biology for targeted drug delivery, contrast enhancement of magnetic resonance imaging, and magnetic hyperthermic treatment [87]. In the case of magnetic hyperthermia, MNPs are heated by external electromagnetic field and dissipate the heat into the surrounding tissue, and tumor cells may be destroyed by means of evolved local heating [88]. For hyperthermia therapy, magnetic nanoparticles are introduced into tumor tissue, and an external electromagnetic field is applied. Tumor tissue is heated up to 43–46 °C [89], resulting in destruction of the tissue, while surrounding healthy cells are not damaged appreciably. The hyperthermia therapy requires magnetic materials with the Curie temperature near 45 °C. Upon reaching the Curie temperature, such magnetic nanoparticles would pass into a paramagnetic state and the hyperthermia heating is stopped. Quantitative characteristics of a

hyperthermic material include such parameters as specific absorption rate (SAR) and specific loss power (SLP). The latter parameter quantifies released thermal energy per unit mass of the magnetic particles. This value should be as high as possible. The efficiency of heat release by $\text{Co}_x\text{Zn}_{1-x}\text{Fe}_2\text{O}_4$ magnetic nanoparticles was, therefore, also investigated in the present study.

Heating profiles of water suspensions of zinc-cobalt ferrites at concentration of 75 mg/mL are shown in Fig. 17a. The initial fast increase in temperature is followed by slower heating and then temperature becomes stable. The presented heating curves indicate clearly that the heating efficiency depends on the zinc content in the magnetic ferrite particles. Under the given conditions, the samples with $x(\text{Zn}) = 0.2$, $x(\text{Zn}) = 0.4$, $x(\text{Zn}) = 0.6$, $x(\text{Zn}) = 0.8$ and $x(\text{Zn}) = 1.0$ are heated to temperatures of 24.13°C, 29.51°C, 45.91°C, 31.49°C and 24.63°C, respectively (Fig. 17b). The temperature range from 43 to 46 °C is considered as the most effective for the successful hyperthermia therapy. The time required for heating the $\text{Co}_{0.4}\text{Zn}_{0.6}\text{Fe}_2\text{O}_4$ sample to the therapeutic

temperature is equal to 39 min (Fig. 17a). The values of SLP were calculated for all the studied $\text{Co}_{1-x}\text{Zn}_x\text{Fe}_2\text{O}_4$ samples, taking into account the initial slopes of the temperature curves vs. time (Fig. 17a). With an increase of zinc content, the SLP values also increase up to $x(\text{Zn}) = 0.6$, and next decrease (Fig. 17c). The maximum value of $\text{SLP} = 2.56 \text{ W/g}$ was found for the sample with $x(\text{Zn}) = 0.6$.

The values of the intrinsic loss power (ILP) were calculated in order to compare the presented data with literature ones. Magnetic field intensity of 100 Oe at the frequency of 100 kHz were taken into account. From the results presented in Fig. 17d, it can be inferred that the ILP values for the synthesized cobalt-zinc ferrites are changed with the Zn content. The sample $\text{Co}_{0.4}\text{Zn}_{0.6}\text{Fe}_2\text{O}_4$ exhibits the maximal value of $\text{ILP} = 0.40 \text{ nH}\cdot\text{m}^2\cdot\text{kg}^{-1}$. This value is 2.7 times higher than the corresponding ILP value of commercial magnetite (Fe_3O_4) equal to $0.15 \text{ nH}\cdot\text{m}^2\cdot\text{kg}^{-1}$. The $\text{Co}_{0.6}\text{Zn}_{0.4}\text{Fe}_2\text{O}_4$ and $\text{Co}_{0.2}\text{Zn}_{0.8}\text{Fe}_2\text{O}_4$ samples exhibit the ILP values of 0.19 and $0.23 \text{ nH}\cdot\text{m}^2\cdot\text{kg}^{-1}$, respectively. These results are also superior as compared with the commercial Fe_3O_4 . The ILP values

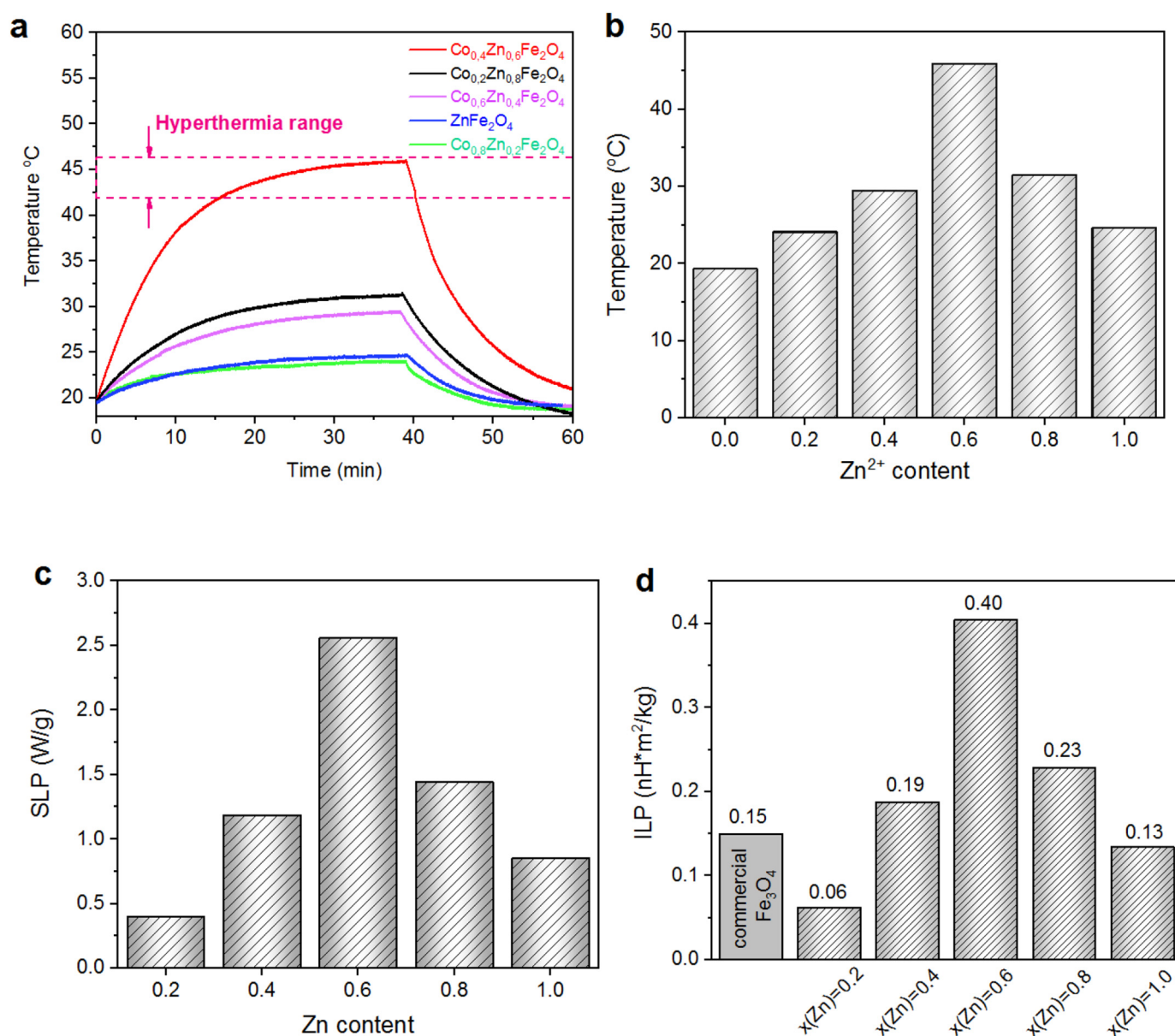


Fig. 17. Results of the magnetic hyperthermia measurements: (a) Induction heating curves of $\text{Co}_x\text{Zn}_{1-x}\text{Fe}_2\text{O}_4$ suspensions in distilled water as a function of the Zn content (process conditions: frequency = 100 kHz; NP concentration = 75 mg/ml); (b) The dependence of the maximum heating temperature of the $\text{Co}_{1-x}\text{Zn}_x\text{Fe}_2\text{O}_4$ suspensions on the zinc content; (c) The specific loss power (SLP) vs. Zn content for the $\text{Co}_{1-x}\text{Zn}_x\text{Fe}_2\text{O}_4$ samples; (d) Intrinsic loss power (ILP) vs. the Zn content in the $\text{Co}_{1-x}\text{Zn}_x\text{Fe}_2\text{O}_4$ samples.

0.06 and 0.13 $\text{nH}\cdot\text{m}^2\cdot\text{kg}^{-1}$ for the samples with $x(\text{Zn}) = 0.2$ and $x(\text{Zn}) = 1.0$, respectively, are lower as compared with the ILP of commercial Fe_3O_4 . This preliminary study shows that the magnetic cobalt-zinc ferrite nanoparticles, synthesized by honey-mediated method, satisfy requirements of the hyperthermia therapy, and are thus promising for use in biomedicine. More detailed future studies are needed to determine if proper adjusting of the magnetic field and the particle concentration will lead to the desired efficient hyperthermal effect.

4. Conclusions

Honey-mediated synthesis of cobalt-zinc ferrite NPs was developed. The obtained NPs were thoroughly characterized by means of XRD, SEM/EDS, TEM, Mössbauer and FTIR techniques. All the samples exhibit a single phase with the spinel cubic structure ($Fd-3m$). It was found that the obtained spinel nanoparticles have crystallite size around 14 ± 2 nm. The Mössbauer spectra of cobalt-zinc ferrites reveal that the Zn content controls the magneto-crystalline anisotropy and the superparamagnetic/ferromagnetic state of the synthesized particles. The force constants of the tetrahedral and octahedral bonds are in the range 2.840–2.974 dyn/cm^2 and 1.470–1.851 dyn/cm^2 respectively. Increase in the Zn content leads to increase of the k_{O} and decrease of k_{T} force constants values. Direct correlation between the Debye temperature and the octahedral force constant was also found for the first time. Adsorption properties of cobalt-zinc ferrites were evaluated in the case of Pb^{2+} removal from water solutions. Adsorption capacity values of the Zn-doped samples vary from 23.10 mg/g (for $\text{Co}_{0.8}\text{Zn}_{0.2}\text{Fe}_2\text{O}_4$) to 289 mg/g (for ZnFe_2O_4). Three isotherm models (Langmuir, Freundlich and Dubinin-Radushkevich) were applied in order to explain adsorption mechanism. The Langmuir equation describes well the experimental results, implying that a monomolecular layer adsorption of Pb^{2+} takes place. The synthesized ferrites were tested for possible application in magnetic hyperthermal therapy. The specific loss power and the ILP coefficients were determined at magnetic field of 100 Oe and the frequency of 100 kHz. The maximum values of the SLP (2.56 W/g) and ILP (0.40 $\text{nH}\cdot\text{m}^2\cdot\text{kg}^{-1}$) parameters were found for the $\text{Co}_{0.4}\text{Zn}_{0.6}\text{Fe}_2\text{O}_4$ sample, which are higher than those of commercial Fe_3O_4 . The obtained results are promising for fabrication of new functional cobalt-zinc ferrites-based materials aimed for practical applications. The developed method for synthesis of cobalt-zinc ferrite nanoparticles can be used as a green technology for the production of nanopowders with desired properties for a wide range of environmental and biomedical applications.

Credit author statement

Tetiana Tatarchuk: Supervision; Ideas; Formulation of overarching research goals and aims; Development of methodology; Sample synthesis; Conducting a research; Visualization; Writing- Original draft preparation; Writing- Reviewing and Editing; **Alexander Shyichuk:** Conducting a research; Writing- Original draft preparation; Writing- Reviewing and Editing; **Zbigniew Sojka:** Transmission electron microscopy observations; Writing- Original draft preparation; **Joanna Gryboś:** Transmission electron microscopy observations; **Mu. Naushad:** Writing- Original draft preparation; Writing- Reviewing and Editing; **Volodymyr Kotsyubynsky:** Mossbauer spectroscopy; Writing- Original draft preparation; **Maria Kowalska:** Adsorption properties determination; **Sylwia Kwiatkowska-Marks:** Adsorption properties determination; **Nazarii Danyliuk:** Magnetic hyperthermia measurements.

Declaration of Competing Interest

The authors declare that they have no known competing financial interests or personal relationships that could have appeared to influence the work reported in this paper.

Acknowledgements

Financial support of this work was obtained from Ministry of Education and Science of Ukraine (project number 0118U000258). Mu. Naushad acknowledges the support from the Distinguished Scientist Fellowship Program (DSFP), King Saud University, Riyadh, Saudi Arabia.

References

- [1] D.H.K. Reddy, Y.-S. Yun, Spinel ferrite magnetic adsorbents: alternative future materials for water purification? *Coord. Chem. Rev.* 315 (2016) 90–111, <https://doi.org/10.1016/j.ccr.2016.01.012>.
- [2] B.I. Kharisov, H.V.R. Dias, O.V. Kharissova, Mini-Review: Ferrite Nanoparticles in the Catalysis, *Arab. J. Chem.* (2014) <https://doi.org/10.1016/j.ARABJC.2014.10.049>.
- [3] N. Ali, H. Zaman, M. Bilal, A.-H.A. Shah, M.S. Nazir, H.M.N. Iqbal, Environmental perspectives of interfacially active and magnetically recoverable composite materials – a review, *Sci. Total Environ.* 670 (2019) 523–538, <https://doi.org/10.1016/j.SCTOTENV.2019.03.209>.
- [4] D.H.K. Reddy, Y.-S. Yun, Spinel ferrite magnetic adsorbents: alternative future materials for water purification? *Coord. Chem. Rev.* 315 (2016) 90–111, <https://doi.org/10.1016/j.ccr.2016.01.012>.
- [5] K.K. Kefeni, B.B. Mamba, T.A.M. Msagati, Application of spinel ferrite nanoparticles in water and wastewater treatment: a review, *Sep. Purif. Technol.* 188 (2017) 399–422, <https://doi.org/10.1016/j.seppur.2017.07.015>.
- [6] P. Kharbanda, T. Madaan, I. Sharma, S. Vashishtha, P. Kumar, A. Chauhan, S. Mittal, J.S. Bangruwa, V. Verma, Ferrites: magnetic materials as an alternate source of green electrical energy, *Heliyon.* 5 (2019), e01151, <https://doi.org/10.1016/j.heliyon.2019.E01151>.
- [7] N. Danyliuk, J. Tomaszewska, T. Tatarchuk, Halloysite nanotubes and halloysite-based composites for environmental and biomedical applications, *J. Mol. Liq.* 309 (2020) 113077, <https://doi.org/10.1016/j.molliq.2020.113077>.
- [8] T. Tatarchuk, I. Mironyuk, V. Kotsyubynsky, A. Shyichuk, M. Myslin, V. Boychuk, Structure, morphology and adsorption properties of titania shell immobilized onto cobalt ferrite nanoparticle core, *J. Mol. Liq.* 297 (2020) 111757, <https://doi.org/10.1016/j.molliq.2019.111757>.
- [9] T. Tatarchuk, M. Naushad, J. Tomaszewska, P. Kosobucki, M. Myslin, H. Vasylyeva, P. Ścigalski, Adsorption of Sr(II) ions and salicylic acid onto magnetic magnesium-zinc ferrites: isotherms and kinetic studies, *Environ. Sci. Pollut. Res.* (2020) <https://doi.org/10.1007/s11356-020-09043-1>.
- [10] T. Tatarchuk, A. Shyichuk, I. Trawczyńska, I. Yaremiy, A.T. Pędziwiatr, P. Kurzydło, B.F. Bogacz, R. Gargula, Spinel cobalt(II) ferrite-chromites as catalysts for H2O2 decomposition: synthesis, morphology, cation distribution and antistructure model of active centers formation, *Ceram. Int.* 46 (2020) 27517–27530, <https://doi.org/10.1016/j.ceramint.2020.07.243>.
- [11] A. Maleki, Z. Hajizadeh, V. Sharifi, Z. Emdadi, A green, porous and eco-friendly magnetic geopolymer adsorbent for heavy metals removal from aqueous solutions, *J. Clean. Prod.* 215 (2019) 1233–1245, <https://doi.org/10.1016/j.jclepro.2019.01.084>.
- [12] A.A. Basheer, New generation nano-adsorbents for the removal of emerging contaminants in water, *J. Mol. Liq.* 261 (2018) 583–593, <https://doi.org/10.1016/j.molliq.2018.04.021>.
- [13] T. Tatarchuk, N. Paliychuk, M. Pacia, W. Kaspera, W. Macyk, A. Kotarba, B.F. Bogacz, A.T. Pędziwiatr, I. Mironyuk, R. Gargula, P. Kurzydło, A. Shyichuk, Structure-redox reactivity relationships in $\text{Co}_{1-x}\text{Zn}_x\text{Fe}_2\text{O}_4$: the role of stoichiometry, *New J. Chem.* 43 (2019) 3038–3049, <https://doi.org/10.1039/c8nj05329d>.
- [14] B.F. Bogacz, R. Gargula, P. Kurzydło, A.T. Pędziwiatr, T. Tatarchuk, N. Paliychuk, Two-level model description of superparamagnetic relaxation in nanoferrites (Co,Zn) Fe_2O_4 , *Acta Phys. Pol. A* 134 (2018) 993–997, <https://doi.org/10.12693/PhysPolA.134.993>.
- [15] S. Raghuvanshi, S.N. Kane, T.R. Tatarchuk, F. Mazaleyrat, Effect of Zn addition on structural, magnetic properties, antistructural modeling of $\text{Co}_{1-x}\text{Zn}_x\text{Fe}_2\text{O}_4$ nano ferrite, *AIP Conf. Proc.* 1953 (2018) 2–6, <https://doi.org/10.1063/1.5032390>.
- [16] D.D. Andhare, S.R. Patade, J.S. Kounsalye, K.M. Jadhav, Effect of Zn doping on structural, magnetic and optical properties of cobalt ferrite nanoparticles synthesized via Co-precipitation method, *Phys. B Condens. Matter.* 583 (2020) 412051, <https://doi.org/10.1016/j.physb.2020.412051>.
- [17] M. Atif, M.W. Asghar, M. Nadeem, W. Khalid, Z. Ali, S. Badshah, Synthesis and investigation of structural, magnetic and dielectric properties of zinc substituted cobalt ferrites, *J. Phys. Chem. Solids* 123 (2018) 36–42, <https://doi.org/10.1016/j.jpcs.2018.07.010>.
- [18] K. Anu, J. Hemalatha, Magnetic and electrical conductivity studies of zinc doped cobalt ferrite nanofluids, *J. Mol. Liq.* 284 (2019) 445–453, <https://doi.org/10.1016/j.molliq.2019.04.018>.
- [19] D.S. Nair, M. Kurian, Heterogeneous catalytic oxidation of persistent chlorinated organics over cobalt substituted zinc ferrite nanoparticles at mild conditions: reaction kinetics and catalyst reusability studies, *J. Environ. Chem. Eng.* 5 (2017) 964–974, <https://doi.org/10.1016/j.jece.2017.01.021>.
- [20] D.S. Nair, M. Kurian, Highly selective synthesis of diphenyl methane via liquid phase benzylation of benzene over cobalt doped zinc nanoferrite catalysts at mild conditions, *J. Saudi Chem. Soc.* 23 (2019) 127–132, <https://doi.org/10.1016/j.jscs.2018.05.011>.
- [21] M. Sundararajan, V. Sailaja, L. Kennedy, J. Vijaya, Photocatalytic degradation of rhodamine B under visible light using nanostructured zinc doped cobalt ferrite, *Kinet. Mech. Chem. Under Int.* 43 (1A) (2017) 540–548, <https://doi.org/10.1016/j.ceramint.2016.09.191>.

- [22] P. Appa Rao, K. Srinivasa Rao, T.R.K. Pydi Raju, G. Kapusetti, M. Choppadandi, M. Chaitanya Varma, K.H. Rao, A systematic study of cobalt-zinc ferrite nanoparticles for self-regulated magnetic hyperthermia, *J. Alloys Compd.* 794 (2019) 60–67, <https://doi.org/10.1016/j.jallcom.2019.04.242>.
- [23] N. Sattarahmady, T. Zare, A.R. Mehdizadeh, N. Azarpira, M. Heidari, M. Lotfi, H. Heli, Dextrin-coated zinc substituted cobalt-ferrite nanoparticles as an MRI contrast agent: in vitro and in vivo imaging studies, *Colloids Surfaces B Biointerfaces*. 129 (2015) 15–20, <https://doi.org/10.1016/j.colsurfb.2015.03.021>.
- [24] M. Madhukara Naik, H.S. Bhojya Naik, G. Nagaraju, M. Vinuth, K. Vinu, R. Viswanath, Green synthesis of zinc doped cobalt ferrite nanoparticles: structural, optical, photocatalytic and antibacterial studies, *Nano-Structures & Nano-Objects*. 19 (2019) 100322, <https://doi.org/10.1016/j.nanos.2019.100322>.
- [25] M.K. Satheeshkumar, E. Ranjith Kumar, C. Srinivas, G. Prasad, S.S. Meena, I. Pradeep, N. Suriyanarayanan, D.L. Sastry, Structural and magnetic properties of CuFe2O4 ferrite nanoparticles synthesized by cow urine assisted combustion method, *J. Magn. Mater.* 484 (2019) 120–125, <https://doi.org/10.1016/j.jmmm.2019.03.128>.
- [26] M. Deepty, C. Srinivas, E.R. Kumar, N.K. Mohan, C.L. Prajapat, T.V.C. Rao, S.S. Meena, A.K. Verma, D.L. Sastry, XRD, EDX, FTIR and ESR spectroscopic studies of co-precipitated Mn-substituted Zn-ferrite nanoparticles, *Ceram. Int.* 45 (2019) 8037–8044, <https://doi.org/10.1016/j.ceramint.2019.01.029>.
- [27] M. Deepty, C. Srinivas, K. Vijaya Babu, E. Ranjith Kumar, S. Singh Meena, C.L. Prajapat, N. Krishna Mohan, D.L. Sastry, Structural and electron spin resonance spectroscopic studies of $MnxZn1-xFe2O4$ ($x = 0.5, 0.6, 0.7$) nanoferrites synthesized by sol-gel auto combustion method, *J. Magn. Mater.* 466 (2018) 60–68, <https://doi.org/10.1016/j.jmmm.2018.06.078>.
- [28] W. Zhu, X. Dong, H. Huang, M. Qi, Iron nanoparticles-based magnetorheological fluids: a balance between MR effect and sedimentation stability, *J. Magn. Mater.* 491 (2019) 165556, <https://doi.org/10.1016/j.jmmm.2019.165556>.
- [29] S.P. Yeap, S.Y. Tia, Induced rapid magnetic sedimentation of stabilized-Fe3O4 nanoparticles by bridging and depletion flocculation, *Chem. Eng. Res. Des.* 142 (2019) 53–61, <https://doi.org/10.1016/j.cherd.2018.12.004>.
- [30] O.P. Bolade, A.B. Williams, N.U. Benson, Green synthesis of iron-based nanomaterials for environmental remediation: A review, *Environ. Nanotechnology, Monit. Manag.* 13 (2020) 100279, <https://doi.org/10.1016/j.enmm.2019.100279>.
- [31] M. Khalaj, M. Kamali, M.E.V. Costa, I. Capela, Green synthesis of nanomaterials - A scientometric assessment, *J. Clean. Prod.* 267 (2020) 122036, <https://doi.org/10.1016/j.jclepro.2020.122036>.
- [32] P. Mondal, A. Anweshan, M.K. Purkait, Green synthesis and environmental application of iron-based nanomaterials and nanocomposite: a review, *Chemosphere*. 259 (2020) 127509, <https://doi.org/10.1016/j.chemosphere.2020.127509>.
- [33] C. Qiu, Y. Hu, Z. Jin, D.J. McClements, Y. Qin, X. Xu, J. Wang, A review of green techniques for the synthesis of size-controlled starch-based nanoparticles and their applications as nanodelivery systems, *Trends Food Sci. Technol.* 92 (2019) 138–151, <https://doi.org/10.1016/j.tifs.2019.08.007>.
- [34] A. Rana, K. Yadav, S. Jagadevan, A comprehensive review on green synthesis of nature-inspired metal nanoparticles: mechanism, application and toxicity, *J. Clean. Prod.* 122880 (2020) <https://doi.org/10.1016/j.jclepro.2020.122880>.
- [35] H. Chandra, P. Kumari, E. Bontempi, S. Yadav, Medicinal plants: treasure trove for green synthesis of metallic nanoparticles and their biomedical applications, *Biocatal. Agric. Biotechnol.* 24 (2020) 101518, <https://doi.org/10.1016/j.bcab.2020.101518>.
- [36] M. Bandeira, M. Giovanela, M. Roesch-Ely, D.M. Devine, J. da Silva Crespo, Green synthesis of zinc oxide nanoparticles: a review of the synthesis methodology and mechanism of formation, *Sustain. Chem. Pharm.* 15 (2020) 100223, <https://doi.org/10.1016/j.scp.2020.100223>.
- [37] A. Si, K. Pal, S. Kralj, G.S. El-Sayyad, F.G. de Souza, T. Narayanan, Sustainable preparation of gold nanoparticles via green chemistry approach for biogenic applications, *Mater. Today Chem.* 17 (2020) 100327, <https://doi.org/10.1016/j.mtchem.2020.100327>.
- [38] P. Das, V.S. Karankar, New avenues of controlling microbial infections through antimicrobial and anti-biofilm potentials of green mono-and multi-metallic nanoparticles: a review, *J. Microbiol. Methods* 167 (2019) 105766, <https://doi.org/10.1016/j.mimet.2019.105766>.
- [39] M.K. Satheeshkumar, E.R. Kumar, C. Srinivas, N. Suriyanarayanan, M. Deepty, C.L. Prajapat, T.V.C. Rao, D.L. Sastry, Study of structural, morphological and magnetic properties of Ag substituted cobalt ferrite nanoparticles prepared by honey assisted combustion method and evaluation of their antibacterial activity, *J. Magn. Mater.* 469 (2019) 691–697, <https://doi.org/10.1016/j.jmmm.2018.09.039>.
- [40] D. Philip, Honey mediated green synthesis of silver nanoparticles, *Spectrochim. Acta Part A Mol. Biomol. Spectrosc.* 75 (2010) 1078–1081, <https://doi.org/10.1016/j.saa.2009.12.058>.
- [41] R. Venu, T.S. Ramulu, S. Anandakumar, V.S. Rani, C.G. Kim, Bio-directed synthesis of platinum nanoparticles using aqueous honey solutions and their catalytic applications, *Colloids Surfaces A Physicochem. Eng. Asp.* 384 (2011) 733–738, <https://doi.org/10.1016/j.colsurfa.2011.05.045>.
- [42] D. Philip, Honey mediated green synthesis of gold nanoparticles, *Spectrochim. Acta Part A Mol. Biomol. Spectrosc.* 73 (2009) 650–653, <https://doi.org/10.1016/j.saa.2009.03.007>.
- [43] R.A. Zayadi, F. Abu Bakar, M.K. Ahmad, Elucidation of synergistic effect of eucalyptus globulus honey and Zingiber officinale in the synthesis of colloidal biogenic gold nanoparticles with antioxidant and catalytic properties, *Sustain. Chem. Pharm.* 13 (2019) 100156, <https://doi.org/10.1016/j.scp.2019.100156>.
- [44] B.S. Bukhari, M.I. Mahwish, Honey mediated microwave assisted sol-gel synthesis of stabilized zirconia nano fibers, *J. Sol-Gel Sci. Technol.* (2018) <https://doi.org/10.1007/s10971-018-4749-0>.
- [45] R.S. Yadav, I. Kufitka, J. Vilcakova, P. Urbánek, M. Machovsky, M. Masař, M. Holek, Structural, magnetic, optical, dielectric, electrical and modulus spectroscopic characteristics of ZnFe2O4 spinel ferrite nanoparticles synthesized via honey-mediated sol-gel combustion method, *J. Phys. Chem. Solids* 110 (2017) 87–99, <https://doi.org/10.1016/j.jpcs.2017.05.029>.
- [46] T. Tatarchuk, A. Shyichuk, I. Mironyuk, M. Naushad, A review on removal of uranium (VI) ions using titanium dioxide based sorbents, *J. Mol. Liq.* 293 (2019) 111563, <https://doi.org/10.1016/j.molliq.2019.111563>.
- [47] D. Ziolkowska, A. Shyichuk, I. Karwasz, M. Witkowska, Adsorption of cationic and anionic dyes onto commercial kaolin, *Adsorpt. Sci. Technol.* 27 (2009) 205–214, <https://doi.org/10.1260/026361709789625306>.
- [48] M. Naushad, A.A. Alqadami, A.A. Al-Kahtani, T. Ahmad, M.R. Awual, T. Tatarchuk, Adsorption of textile dye using Para-aminobenzoic acid modified activated carbon: kinetic and equilibrium studies, *J. Mol. Liq.* 296 (2019) 112075, <https://doi.org/10.1016/j.molliq.2019.112075>.
- [49] H. Zhang, C. Li, L. Lyu, C. Hu, Surface oxygen vacancy inducing peroxy monosulfate activation through electron donation of pollutants over cobalt-zinc ferrite for water purification, *Appl. Catal. B Environ.* 270 (2020) 118874, <https://doi.org/10.1016/j.apcatb.2020.118874>.
- [50] T. Tatarchuk, N. Paliychuk, R.B. Bitra, A. Shyichuk, M. Naushad, I. Mironyuk, D. Ziolkowska, Adsorptive removal of toxic methylene blue and acid Orange 7 dyes from aqueous medium using cobalt-zinc ferrite nanoadsorbents, *Desalin. Water Treat.* 150 (2019) 374–385, <https://doi.org/10.5004/dwt.2019.23751>.
- [51] L.P. Lingamdinne, J.R. Koduru, Y.-L. Choi, Y.-Y. Chang, J.-K. Yang, Studies on removal of Pb(II) and Cr(III) using graphene oxide based inverse spinel nickel ferrite nanocomposite as sorbent, *Hydrometallurgy*. 165 (2016) 64–72, <https://doi.org/10.1016/j.hydromet.2015.11.005>.
- [52] E. Cheraghpoor, M. Pakshir, Process optimization and modeling of Pb(II) ions adsorption on chitosan-conjugated magnetite nano-biocomposite using response surface methodology, *Chemosphere*. 260 (2020) 127560, <https://doi.org/10.1016/j.chemosphere.2020.127560>.
- [53] T. Perez, D. Pasquini, A. de Faria Lima, E.V. Rosa, M.H. Sousa, D.A. Cerqueira, L.C. de Moraes, Efficient removal of lead ions from water by magnetic nanosorbents based on manganese ferrite nanoparticles capped with thin layers of modified biopolymers, *J. Environ. Chem. Eng.* 7 (2019) 102892, <https://doi.org/10.1016/j.jece.2019.102892>.
- [54] K. Al Yaqoob, M. Bououdina, M.S. Akhter, B. Al Najjar, J.J. Vijaya, Selectivity and efficient Pb and Cd ions removal by magnetic MFe2O4 (M=co, Ni, cu and Zn) nanoparticles, *Mater. Chem. Phys.* 232 (2019) 254–264, <https://doi.org/10.1016/j.matchemphys.2019.04.077>.
- [55] R. Asadi, H. Abdollahi, M. Gharabaghi, Z. Boroumand, Effective removal of Zn (II) ions from aqueous solution by the magnetic MnFe2O4 and CoFe2O4 spinel ferrite nanoparticles with focuses on synthesis, characterization, adsorption, and desorption, *Adv. Powder Technol.* 31 (2020) 1480–1489, <https://doi.org/10.1016/j.apt.2020.01.028>.
- [56] M. Kumar, H.S. Dosanjh, H. Singh, Removal of lead and copper metal ions in single and binary systems using biopolymer modified spinel ferrite, *J. Environ. Chem. Eng.* 6 (2018) 6194–6206, <https://doi.org/10.1016/j.jece.2018.09.054>.
- [57] J. R., J. Simultaneous removal of binary dye from textile effluent using cobalt ferrite-alginate nanocomposite: Performance and mechanism, *Microchem. J.* 145 (2019) 791–800, <https://doi.org/10.1016/j.microc.2018.11.047>.
- [58] E.P. Muniz, L.S.D. de Assunção, L.M. de Souza, J.J.K. Ribeiro, W.P. Marques, R.D. Pereira, P.S.S. Porto, J.R.C. Proveti, E.C. Passamani, On cobalt ferrite production by sol-gel from orange fruit residue by three related procedures and its application in oil removal, *J. Clean. Prod.* 265 (2020) 121712, <https://doi.org/10.1016/j.jclepro.2020.121712>.
- [59] A. Dey, R. Singh, M.K. Purkait, Cobalt ferrite nanoparticles aggregated schwertmannite: a novel adsorbent for the efficient removal of arsenic, *J. Water Process Eng.* 3 (2014) 1–9, <https://doi.org/10.1016/j.jwpe.2014.07.002>.
- [60] Y. Zhang, T. Yan, L. Yan, X. Guo, L. Cui, Q. Wei, B. Du, Preparation of novel cobalt ferrite/chitosan grafted with graphene composite as effective adsorbents for mercury ions, *J. Mol. Liq.* 198 (2014) 381–387, <https://doi.org/10.1016/j.molliq.2014.07.043>.
- [61] C.M. Park, Y.M. Kim, K.-H. Kim, D. Wang, C. Su, Y. Yoon, Potential utility of graphene-based spinel ferrites as adsorbent and photocatalyst for removing organic/inorganic contaminants from aqueous solutions: a mini review, *Chemosphere*. 221 (2019) 392–402, <https://doi.org/10.1016/j.chemosphere.2019.01.063>.
- [62] C. Wu, Y. Xu, S. Xu, J. Tu, C. Tian, Z. Lin, Enhanced adsorption of arsenate by spinel zinc ferrite nano particles: effect of zinc content and site occupation, *J. Environ. Sci.* 79 (2019) 248–255, <https://doi.org/10.1016/j.jes.2018.09.010>.
- [63] G. Sharma, M. Naushad, Adsorptive removal of noxious cadmium ions from aqueous medium using activated carbon/zirconium oxide composite: isotherm and kinetic modelling, *J. Mol. Liq.* 310 (2020) 113025, <https://doi.org/10.1016/j.molliq.2020.113025>.
- [64] J.T. Jang, J. Lee, J. Seon, E. Ju, M. Kim, Y. Il Kim, M.G. Kim, Y. Takemura, A.S. Arbab, K.W. Kang, K.H. Park, S.H. Paek, S. Bae, Giant magnetic heat induction of magnesium-doped γ -Fe2O3 Superparamagnetic nanoparticles for completely killing tumors, *Adv. Mater.* 30 (2018) 1–8, <https://doi.org/10.1002/adma.201704362>.
- [65] M. Kallumadil, M. Tada, T. Nakagawa, M. Abe, P. Southern, Q.A. Pankhurst, Suitability of commercial colloids for magnetic hyperthermia, *J. Magn. Mater.* 321 (2009) 1509–1513, <https://doi.org/10.1016/j.jmmm.2009.02.075>.
- [66] I. Kasprzyk, J. Depciuch, D. Grabek-Lejko, M. Parlinska-Wojtan, FTIR-ATR spectroscopy of pollen and honey as a tool for unifloral honey authentication. The case study of rape honey, *Food Control* 84 (2018) 33–40, <https://doi.org/10.1016/j.foodcont.2017.07.015>.
- [67] Y. Riswahyuli, A. Rohman, F.M.C.S. Setyabudi, S. Raharjo, Indonesian wild honey authenticity analysis using attenuated total reflectance-fourier transform infrared (ATR-FTIR) spectroscopy combined with multivariate statistical techniques, *Heliyon*. 6 (2020), e03662, <https://doi.org/10.1016/j.heliyon.2020.e03662>.

- [68] H. Elrasheid Tahir, G. Komla Mahunu, M. Arslan, L. Zhihua, Z. Wen, Z. Xiaobo, A. Adam Mariod, S. Jiyong, Feasibility study for the use of colorimetric sensor arrays, NIR and FT-IR spectroscopy in the quantitative analysis of volatile components in honey, *Microchem. J.* 160 (2021) 105730, <https://doi.org/10.1016/j.microc.2020.105730>.
- [69] O. Anjos, M.G. Campos, P.C. Ruiz, P. Antunes, Application of FTIR-ATR spectroscopy to the quantification of sugar in honey, *Food Chem.* 169 (2015) 218–223, <https://doi.org/10.1016/j.foodchem.2014.07.138>.
- [70] I. Sharifi, H. Shokrollahi, Nanostructural, magnetic and Mössbauer studies of nanosized Co_{1-x}ZnxFe₂O₄ synthesized by co-precipitation, *J. Magn. Magn. Mater.* 324 (2012) 2397–2403, <https://doi.org/10.1016/j.jmmm.2012.03.008>.
- [71] T.E. Torres, E. Lima, A. Mayoral, A. Ibarra, C. Marquina, M.R. Ibarra, G.F. Goya, Validity of the Néel-Arrhenius model for highly anisotropic CoxFe_{3-x}O₄ nanoparticles, *J. Appl. Phys.* 118 (2015) <https://doi.org/10.1063/1.4935146>.
- [72] K. Hasz, Y. Ijiri, K.L. Krycka, J.A. Borchers, R.A. Booth, S. Oberdick, S.A. Majetich, Particle moment canting in CoFe₂O₄ nanoparticles, *Phys. Rev. B - Condens. Matter Mater. Phys.* 90 (2014) 1–5, <https://doi.org/10.1103/PhysRevB.90.180405>.
- [73] G. Muscas, D. Peddis, M. Cobianchi, A. Lascialfari, C. Cannas, A. Musinu, A. Omelyanchik, V. Rodionova, D. Fiorani, V. Marnelli, Magnetic interactions versus magnetic anisotropy in spinel ferrite nanoparticles, *IEEE Magn. Lett.* 10 (2019) 1–5, <https://doi.org/10.1109/LMAG.2019.2956908>.
- [74] B.H. Liu, J. Ding, Z.L. Dong, C.B. Boothroyd, J.H.B. Yin, J. Yi, Microstructural evolution and its influence on the magnetic properties of CoFe₂O₄ powders during mechanical milling, *Phys. Rev. B* 74 (2006) 184427, <https://doi.org/10.1103/PhysRevB.74.184427>.
- [75] T. Tatarchuk, A. Shyichuk, J. Lamkiewicz, J. Kowalik, Inversion degree, morphology and colorimetric parameters of cobalt aluminate nanopigments depending on reductant type in solution combustion synthesis, *Ceram. Int.* (2020) <https://doi.org/10.1016/j.ceramint.2020.02.269>.
- [76] T. Tatarchuk, M. Bououdina, N. Paliychuk, Structural characterization and antistructure modeling of cobalt-substituted zinc ferrites, *J. Alloy. Compd.* 694 (15) (2017) 777–791, <https://doi.org/10.1016/j.jallcom.2016.10.067>.
- [77] T. Tatarchuk, M. Bououdina, W. Macyk, O. Shyichuk, N. Paliychuk, I. Yaremiy, B. Al-Najar, M. Pacia, Structural, Optical, and Magnetic Properties of Zn-Doped CoFe₂O₄ Nanoparticles, *Nanoscale Res. Lett.* 12 (2017) <https://doi.org/10.1186/s11671-017-1899-x>.
- [78] M. Naushad, Surfactant assisted nano-composite cation exchanger: development, characterization and applications for the removal of toxic Pb²⁺ from aqueous medium, *Chem. Eng. J.* 235 (2014) 100–108, <https://doi.org/10.1016/j.cej.2013.09.013>.
- [79] L. Sellaoui, F. Edi Soetaredjo, S. Ismadji, É. Cláudio Lima, G.L. Dotto, A. Ben Lamine, A. Erto, New insights into single-compound and binary adsorption of copper and lead ions on a treated sea mango shell: experimental and theoretical studies, *Phys. Chem. Chem. Phys.* 19 (2017) 25927–25937, <https://doi.org/10.1039/c7cp03770h>.
- [80] L. Sellaoui, G.L. Dotto, E.C. Peres, Y. Benguerba, É.C. Lima, A. Ben Lamine, A. Erto, New insights into the adsorption of crystal violet dye on functionalized multi-walled carbon nanotubes: experiments, statistical physics and COSMO-RS models application, *J. Mol. Liq.* 248 (2017) 890–897, <https://doi.org/10.1016/j.molliq.2017.10.124>.
- [81] Z. Li, L. Sellaoui, G. Luiz Dotto, A. Bonilla-Petriciolet, A. Ben Lamine, Understanding the adsorption mechanism of phenol and 2-nitrophenol on a biopolymer-based biochar in single and binary systems via advanced modeling analysis, *Chem. Eng. J.* 371 (2019) 1–6, <https://doi.org/10.1016/j.cej.2019.04.035>.
- [82] T. Tatarchuk, M. Myslin, I. Lapchuk, A. Shyichuk, A.P. Murthy, R. Gargula, P. Kurzydło, B.F. Bogacz, A.T. Pędziwiatr, Magnesium-zinc ferrites as magnetic adsorbents for Cr (VI) and Ni(II) ions removal: cation distribution and antistructure modeling, *Chemosphere.* 129414 (2020) <https://doi.org/10.1016/j.chemosphere.2020.129414>.
- [83] J. Portier, G. Campet, J. Etourneau, M.C.R. Shastri, B. Tanguy, A simple approach to materials design: role played by an ionic-covalent parameter based on polarizing power and electronegativity, *J. Alloys Compd.* 209 (1994) 59–64, [https://doi.org/10.1016/0925-8388\(94\)91076-6](https://doi.org/10.1016/0925-8388(94)91076-6).
- [84] M. Lenglet, Iono-covalent character of the metal-oxygen bonds in oxides: a comparison of experimental and theoretical data, *Act. Passiv. Electron. Components.* 27 (2004) 1–60, <https://doi.org/10.1080/0882751031000116142>.
- [85] R.D. Shannon, Revised effective ionic radii and systematic studies of interatomic distances in halides and Chalcogenides, *Acta Crystallogr. Sect. A.* (1976) 751–767, <https://doi.org/10.1107/S0567739476001551>.
- [86] Y. Zhang, Electronegativities of elements in valence states and their applications. 1. Electronegativities of elements in valence states, *Inorg. Chem.* 21 (1982) 3886–3889, <https://doi.org/10.1021/ic00141a005>.
- [87] A. Manohar, D.D. Geleta, C. Krishnamoorthi, J. Lee, Synthesis, characterization and magnetic hyperthermia properties of nearly monodisperse CoFe₂O₄ nanoparticles, *Ceram. Int.* (2020) <https://doi.org/10.1016/j.ceramint.2020.07.298>.
- [88] I. Raouf, S. Khalid, A. Khan, J. Lee, H.S. Kim, M.-H. Kim, A review on numerical modeling for magnetic nanoparticle hyperthermia: Progress and challenges, *J. Therm. Biol.* 91 (2020) 102644, <https://doi.org/10.1016/j.jtherbio.2020.102644>.
- [89] R.R. Koli, N.G. Deshpande, D.S. Kim, A.R. Shelke, A.V. Fulari, V.J. Fulari, H.K. Cho, Tailoring the magnetic hyperthermia performances of gram-bean-extract-mediated highly disperse MFe₂O₄ (M = Fe, Ni, Mn) nanoferrites, *Ceram. Int.* (2020) <https://doi.org/10.1016/j.ceramint.2020.06.210>.
- [90] B.-L. Zhang, W. Qiu, P.-P. Wang, Y.-L. Liu, J. Zou, L. Wang, J. Ma, Mechanism study about the adsorption of Pb(II) and Cd(II) with iron-trimesic metal-organic frameworks, *Chem. Eng. J.* 385 (2020) 123507, <https://doi.org/10.1016/j.cej.2019.123507>.
- [91] Y.-J. Tu, C.-F. You, M.-H. Chen, Y.-P. Duan, Efficient removal/recovery of Pb onto environmentally friendly fabricated copper ferrite nanoparticles, *J. Taiwan Inst. Chem. Eng.* 71 (2017) 197–205, <https://doi.org/10.1016/j.jtice.2016.12.006>.
- [92] X. Luo, Z. Huang, J. Lin, X. Li, J. Qiu, J. Liu, X. Mao, Hydrothermal carbonization of sewage sludge and in-situ preparation of hydrochar/MgAl-layered double hydroxides composites for adsorption of Pb(II), *J. Clean. Prod.* 258 (2020) 120991, <https://doi.org/10.1016/j.jclepro.2020.120991>.
- [93] Z. Niu, W. Feng, H. Huang, B. Wang, L. Chen, Y. Miao, S. Su, Green synthesis of a novel Mn–Zn ferrite/biochar composite from waste batteries and pine sawdust for Pb²⁺ removal, *Chemosphere.* 252 (2020) 126529, <https://doi.org/10.1016/j.chemosphere.2020.126529>.
- [94] N. Kaur, M. Kaur, D. Singh, Fabrication of mesoporous nanocomposite of graphene oxide with magnesium ferrite for efficient sequestration of Ni (II) and Pb (II) ions: adsorption, thermodynamic and kinetic studies, *Environ. Pollut.* 253 (2019) 111–119, <https://doi.org/10.1016/j.envpol.2019.05.145>.
- [95] Y. Yuan, W. Zhan, F. Jia, S. Song, Multi-edged molybdenite achieved by thermal modification for enhancing Pb(II) adsorption in aqueous solutions, *Chemosphere.* 251 (2020) 126369, <https://doi.org/10.1016/j.chemosphere.2020.126369>.
- [96] X. Zhang, Y. Huang, X. He, J. Lin, X. Yang, D. Li, M. Yu, C. Yu, C. Tang, Synergistic adsorption of Pb(II) ions by Fe₃O₄ nanoparticles-decorated porous BN nanofibers, *Colloids Surfaces A Physicochem. Eng. Asp.* 589 (2020) 124400, <https://doi.org/10.1016/j.colsurfa.2019.124400>.
- [97] A.A. Alqadami, M. Naushad, Z.A. AlOthman, M. Alsuhybani, M. Algamdi, Excellent adsorptive performance of a new nanocomposite for removal of toxic Pb(II) from aqueous environment: adsorption mechanism and modeling analysis, *J. Hazard. Mater.* 389 (2020) 121896, <https://doi.org/10.1016/j.jhazmat.2019.121896>.